Geometric influences on the regional organization of the mammalian brain

James C. Pang[1]*, Peter A. Robinson[2], Kevin M. Aquino[3], Priscila T. Levi[1], Alexander Holmes[1], Marija Markicevic[4], Xilin Shen[4], Thomas Funck[5,6], Nicola Palomero-Gallagher[6,7], Ru Kong[8,9,10,11], B.T. Thomas Yeo[8,9,10,11,12], Jeggan Tiego[1], Mark A. Bellgrove[1], R Todd Constable[4,13], Evelyn Lake[4,13], Michael Breakspear[14,15], Alex Fornito[1]

[1]School of Psychological Sciences, The Turner Institute for Brain and Mental Health, and Monash Biomedical Imaging, Monash University, Clayton, Victoria, Australia

[2]School of Physics, University of Sydney, Sydney, New South Wales, Australia

[3]BrainKey Inc., San Francisco, California, USA

[4]Department of Radiology and Biomedical Imaging, Yale School of Medicine, New Haven, Connecticut, USA

[5]Center for the Developing Brain, Child Mind Institute, New York, New York, USA

[6]Institute of Neuroscience and Medicine (INM-1), Research Centre Jülich, Jülich, Germany

[7]C. & O. Vogt Institute of Brain Research, Heinrich-Heine-University Düsseldorf, Düsseldorf, Germany

[8]Centre for Sleep and Cognition & Centre for Translational MR Research, Yong Loo Lin School of Medicine, National University of Singapore, Singapore, Singapore

[9]Department of Medicine, Human, Longevity Translational Research Programme, Human Potential Translational Research Programme & Institute for Digital Medicine (WisDM), Yong Loo Lin School of Medicine, National University of Singapore, Singapore, Singapore

[10]Department of Electrical and Computer Engineering, National University of Singapore, Singapore, Singapore

[11]N.I Institute for Health, National University of Singapore, Singapore, Singapore

[12]Integrative Sciences and Engineering Programme (ISEP), National University of Singapore, Singapore, Singapore

[13]Department of Biomedical Engineering, Yale University, New Haven, Connecticut, USA

[14]School of Psychological Sciences, College of Engineering, Science and the Environment, University of Newcastle, Callaghan, New South Wales, Australia

[15]School of Medicine and Public Health, College of Health, Medicine and Wellbeing, University of Newcastle, Callaghan, New South Wales, Australia

*Corresponding author. Email: james.pang1@monash.edu

Abstract

The mammalian brain is comprised of anatomically and functionally distinct regions. Substantial work over the past century has pursued the generation of ever-more accurate maps of regional boundaries, using either expert judgement or data-driven clustering of functional, connectional, and/or architectonic properties. However, these approaches are often purely descriptive, have

limited generalizability, and do not elucidate the underlying generative mechanisms that shape the regional organization of the brain. Here, we develop a novel approach that leverages a simple, hierarchical principle for generating a multiscale parcellation of any brain structure in any mammalian species using only its geometry. We show that this approach yields regions at any resolution scale that are more homogeneous than those defined in nearly all existing benchmark brain parcellations in use today across hundreds of anatomical, functional, cellular, and molecular brain properties measured in humans, macaques, marmosets, and mice. We additionally show how our method can be generalized to previously unstudied mammalian species for which no parcellations exist. Finally, we demonstrate how our approach captures the essence of a simple, hierarchical reaction-diffusion mechanism, in which the geometry of a brain structure shapes the spatial expression of putative patterning molecules linked to the formation of distinct regions through development. Our findings point to a highly conserved and universal influence of geometry on the regional organization of the mammalian brain.

Introduction

Over 100 years ago, Brodmann famously used variations in cytoarchitecture to subdivide (or parcellate) the human cerebral cortex into 43 discrete regions[1], which he considered to be "specific morphological organs" (p. 251), each representing an "exclusive individual function that is different from those of other organs" (pp. 251–252). His proposal—that the brain is composed of anatomically and functionally specialized subregions—has fundamentally influenced a century of subsequent research[2,3], such that the prevailing orthodoxy in contemporary neuroscience is that coordinated behaviour arises from interactions between these discrete, specialized areas[4,5].

Despite the popularity of this paradigm, accurate and reliable delineation of regional boundaries has been challenging. Different anatomists have proposed their own cytoarchitectonic parcellations that differ both in the number of areas defined and the anatomical locations of their boundaries[6]. This variability has led some to question the validity, reliability, and utility of discrete cytoarchitectonic borders, particularly outside sharply delimited primary sensorimotor cortices[7–9]. More recent work has leveraged advances in non-invasive techniques, such as magnetic resonance imaging (MRI), to statistically cluster brain locations according to similarities in microstructural, anatomical, connectivity, and functional profiles[10–13]. This work has culminated in a recent flagship study by the Human Connectome Project (HCP)[14] that synthesized multimodal measures to define 180 discrete regions per cortical hemisphere[2]—a >4-fold increase in the number of regions originally defined by Brodmann.

This body of research has been foundational to our understanding of regional specialization in the brain, but it is limited in several key respects. First, all existing parcellations assume that discrete regions are separated by sharp transitions in brain structure and/or function, but many anatomists[7], including Brodmann himself[1], have observed that many areas of the primate cortex show more graded architectonic transitions (see also refs.[15–17]). Second, the regional borders defined according to different properties (e.g., cytoarchitecture, myeloarchitecture, chemoarchitecture, brain function) do not always coincide[6,18], raising questions about which specific property should be prioritized. Third, the functional boundaries of many putative regions defined at any given scale can be malleable, shifting over time in accordance with changing cognitive demands[19–21]. Fourth, most parcellations are defined at a single spatial resolution when, in fact, the brain shows a non-trivial anatomical and functional organization that spans multiple resolution scales[22–24], including those that are supra-regional (e.g., broad cortical "types" of laminar differentiation[25–29] and

distributed, large-scale networks[30–32]) and infra-regional (e.g., columns and hypercolumns[33]). Accordingly, multiple, spatially overlapping modes of structural and functional organization are evident even within regions with well-defined borders, such as V1[34], or those with clear subnuclear structure such as the thalamus[35]. Finally, nearly all existing approaches to brain parcellation are purely descriptive, identifying boundaries between regions according to expert or statistical clustering of patterns in data without any links to an underlying generative mechanism (for exceptions, see refs[36–38]). Such approaches rely on complex data pipelines that are heavily influenced by investigator choices[10], complicating attempts to inter-relate and replicate findings across different contexts. Together, these considerations suggest that many traditional approaches do not yield brain parcellations that generalize across different contexts, resolutions, individuals, brain structures, and species.

Here, we address these limitations by developing a simple, hierarchical, and geometric approach for regional parcellation that captures the essence of key physical constraints on physiological processes that shape the regional organization of the brain. Rather than trying to cluster different brain features into a statistically optimal solution, our approach only requires a model of the geometry of a brain structure as input and can be used as a unified parcellation method for any structure in any species and at any resolution scale. The method provides a direct mapping between discrete and more graded accounts of brain architecture, whilst also offering an intrinsically multiscale description of regional organization. We show that this simple method yields regions with more homogeneous anatomical, functional, cellular, and molecular properties than nearly all existing benchmark parcellations in use today. We then show how our approach aligns naturally with a classical reaction-diffusion mechanism of patterning substances that play an important, and perhaps minimally sufficient role, in shaping the initial blueprint of regional organization in the brain.

A hierarchical, geometric approach for brain parcellation

Early regionalization of brain structures is shaped by morphogens, which are secreted from specific patterning centers and diffuse through the developing cortical primordium along spatially continuous gradients[39–41]. For instance, in the midbrain and hindbrain, highly conserved gradients of *Hox* genes are sufficient to sharply delineate distinct expression domains, called prosomeres, that give rise to subdivisions of the diencephalon and secondary prosencephalon[42]. In the cortex, morphogens, such as fibroblast growth factor 8 (FGF8), Wnt, and Sonic Hedgehog (Shh), trigger the subsequent expression of distinct transcription factors (e.g., *Pax6*, *Emx2*, *Couptf1*) that further drive areal specification[43–49]. The superposition of these expression gradients spatially organizes neurogenic and other developmental dynamics, creating a rudimentary blueprint of areal identity that is gradually refined by thalamic innervation and activity-dependent mechanisms[48,50–54].

The expression gradients formed by morphogens and other patterning factors predominantly align with the rostrocaudal, dorsoventral, and mediolateral axes of the developing telencephalon[50,51,55–57]. As such, they correspond to the cardinal axes of geometric variation in brain structure, which are formally described by the low-order geometric eigenmodes of the cortex derived from a mathematical decomposition of cortical geometry that is comparable to Fourier decomposition[58,59] (see details below). The equivalence between the expression gradients and geometric eigenmodes arises because the geometry of a medium shapes the spatial patterns that arise from the diffusion and interactions of any molecules within it, as dictated by Turing's classical reaction-diffusion equations[41,60]. The low-order eigenmodes are the least physically stable in generic reaction-

diffusion systems and are therefore the first patterns to be expressed[61]. The preponderance of such patterns in early expression gradients of the developing brain[51] thus arises from the physical constraints that geometry imposes on molecular dynamics.

We leverage this constraining effect of geometry to devise a simple algorithm for regional parcellation. The algorithm captures the essential features of a hypothesized set of reaction-diffusion processes that shape the regional organization of the brain, without having to specify the full set of biophysical details of the molecular interactions involved. We begin by describing the application of our algorithm to the left hemisphere of the human neocortex, the surface geometry of which is approximated by a triangular mesh (with 32,492 vertices) derived from a population-average template extracted from T1-weighted (T1w) MRI (Fig. 1A, top left). First, we calculate the surface's geometric eigenmodes by solving the Helmholtz equation,

$$\Delta\psi = -\lambda\psi, \tag{1}$$

where Δ is the Laplace-Beltrami operator (LBO), which accounts for the spatial relationships between vertices on the surface mesh (see 'Derivation of geometric eigenmodes' in Methods), and $\psi = \{\psi_1, \psi_2, \ldots\}$ is the family of geometric eigenmodes with corresponding eigenvalues, $\lambda = \{\lambda_1, \lambda_2, \ldots\}$. The eigenvalues are ordered sequentially and correspond to the effective spatial wavelength of each eigenmode, with $\lambda_1 \approx 0$ being the smallest eigenvalue and ψ_1 the corresponding eigenmode with the longest spatial wavelength (i.e., a spatially uniform or constant eigenmode).

The nodal lines of the eigenmodes (i.e., points with zero magnitude) partition the cortex into positive and negative domains of approximately equal sizes. We use the first non-constant eigenmode ψ_2 with eigenvalue λ_2 to partition the cortex into two subregions along the major rostrocaudal axis (Fig. 1A, top middle and right), as an initial approximation of regional boundaries at the coarsest resolution scale. This eigenmode defines the dominant axis of shape variation and it is the least physically stable, meaning that it will be the first spatial pattern expressed in a reaction-diffusion process[61]. This physical property aligns with experimental evidence that most patterning molecules identified to date are expressed along rostrocaudal gradients[51].

After the initial partition of the cortex along the nodal line of ψ_2 (Fig. 1A, top), we repeat the process successively on each new subregion over multiple iterations to generate a parcellation of any arbitrary scale (Fig. 1A, bottom). This hierarchical bipartition naturally yields parcellations with 2^N parcels, where N is the number of iterations (Fig. 1B). To derive a parcellation comprising any arbitrary number of regions (from 1 to 2^N), we rely on a heuristic that uses the eigenvalues of the resulting sub-regional eigenmodes to prioritize sub-divisions with the smallest eigenvalues (see Supplementary Figs 1A–B and 'Hierarchical partitioning' in Methods). This iterative procedure, based on recursive bipartition, mimics the developmental processes that shape numerous hierarchically organized, multiscale biological systems, such as limbs and digits, bronchial trees, vascular networks, and segmented body plans, in which tissue elements emerge through the successive branching or division of previous ones[60,62–66]. Such a process has also been implicated in brain development and evolution; for instance, the neural tube divides into the spinal cord and cerebral vesicles (hindbrain, midbrain, and forebrain), the vesicles into neuromeres, and the neuromeres into smaller sub-fields across several resolution scales[67,68]. Critically, tissue geometry constrains the precise way in which these bipartitions occur[69].

Our simple algorithm rests on the assumption that geometric constraints and recursive bipartition capture the essential features of the complex cascade of developmental processes that shape the regional organization of the brain. In the following sections, we show how our simplification of

this process allows us to easily generalize our approach to any brain structure, resolution scale, and species, given a model of brain geometry either derived from MRI or alternative methods (e.g., microscopy). We then show more directly how our algorithm captures the core elements of a hierarchical reaction-diffusion process.

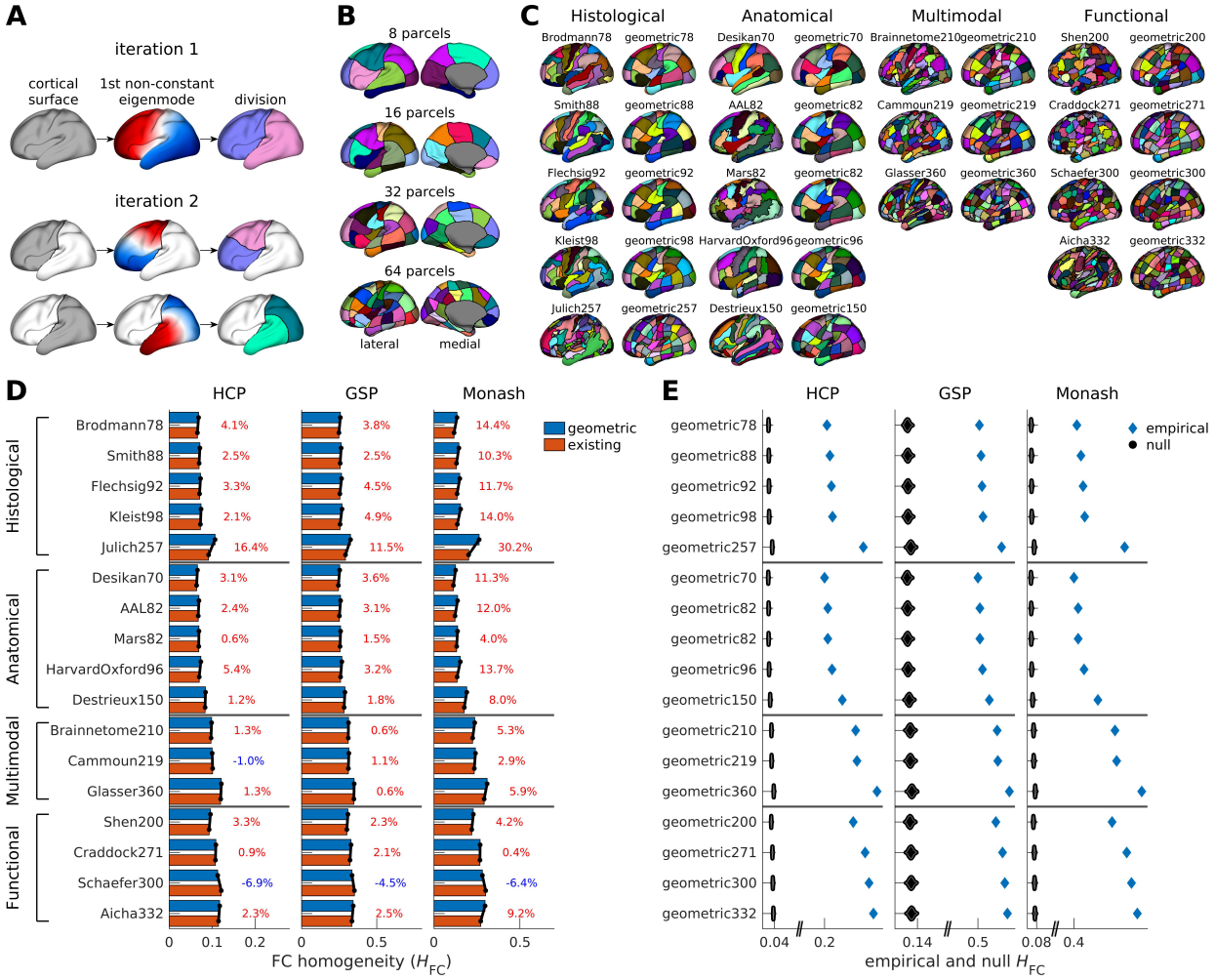

Fig. 1. Hierarchical geometric parcellation of the human neocortex. (**A**) Schematic diagram of our iterative, hierarchical approach. In the first iteration, we divide the cortex into two subregions according to the nodal line of the first non-constant geometric eigenmode (white area, middle panel). In the second iteration, we repeat the process, this time by taking the first non-constant eigenmode estimated separately for the two subregions defined in the first iteration. This process is iterated several times to achieve a desired parcellation resolution, separately for the left and right hemispheres. (**B**) Example multiscale geometric parcellations with 8, 16, 32, and 64 parcels (from top to bottom). (**C**) 17 existing benchmark parcellations and corresponding geometric parcellations with matched number of parcels. The number beside the parcellation's name denotes the total number of parcels across both hemispheres (e.g., Brodmann78 has 78 parcels in total across the left and right hemispheres). (**D**) Regional homogeneity based on FC (H_{FC}) from the HCP, GSP, and Monash datasets. The numbers represent the percentage difference between the geometric and existing parcellations, where positive/red indicates superior performance for geometric parcellations. (**E**) Empirical and null H_{FC} of the counterpart geometric parcellations in Fig. 1C based on 1000 randomized FCs. The blue diamonds correspond to the empirical H_{FC} and the black dots correspond to the null data. Note that the scale of the x-axes is discontinuous (marked by the diagonal lines) because of the difference in magnitude of the empirical and null data. Each geometric parcellation showed significantly higher empirical H_{FC} than the null data (two-sided p-value <0.001).

Geometric parcellations yield functionally, cellularly, and molecularly homogeneous regions

We now investigate the degree to which our geometric parcellations accurately capture the organizational properties of the human neocortex. This accuracy is most commonly determined by the degree to which each region defines a homogeneous set of point-wise (i.e., vertex or voxel) measures[12,70–73], with homogeneity commonly defined in relation to inter-vertex functional coupling (FC) (i.e., average within-region FC; see 'Calculation of regional homogeneity' in Methods). We follow this approach and quantify parcel-level FC homogeneity, H_{FC}, as measured with resting-state functional magnetic resonance imaging (fMRI), in three independent datasets comprising a total of 2259 individuals [i.e., the Human Connectome Project (HCP)[14]; the Genomics Superstructure Project (GSP)[74]; and a dataset acquired in-house at Monash University (Monash)[75]]. We benchmark H_{FC} with respect to 17 existing cortical parcellations that are widely used in the field and that have been constructed in diverse ways, including through the use of histological criteria (Histological), anatomical landmarks (Anatomical), multimodal imaging (Multimodal), or data-driven clustering of resting-state FC (Functional); see Fig. 1C, Supplementary Table 1, and 'Benchmark brain parcellations' in Methods. For each existing parcellation, we generate a corresponding geometric parcellation with the same number of parcels specific to the left and right hemispheres to ensure fair comparison.

Figure 1D shows that our method yields parcels with higher homogeneity than 15 of the 17 benchmark parcellations based on FC data from the HCP dataset and 16 of the 17 in the GSP and Monash datasets (Fig. 1D). The Cammoun219 atlas shows higher H_{FC} than the geometric parcellation only in the HCP dataset, but the difference is minimal (1.0%). The only benchmark parcellation with consistently and notably higher H_{FC} is the Schaefer300 atlas, which relies on extensive fMRI training data and a sophisticated clustering approach[76] that is much more complex than our method.

Figure 1C indicates that, at any given scale, the geometric parcellations resemble an approximately uniform grid (Supplementary Figs 1B) with highly uniform parcels (Supplementary Figs 1C–D) that are unlike the less regular regional borders seen in other parcellations. This grid-like structure partly arises from the hierarchical partitioning of our procedure. It mirrors similar organizational motifs observed in inter-regional axonal projections[77] and may be considered analogous to a rectilinear map of areal organization that results from a superposition of continuous expression gradients of key patterning molecules[51,53].

To ensure that the strong performance of our geometric approach is not merely driven by the uniformity of its parcels, we conduct two analyses. First, we show that differences in H_{FC} between the geometric and existing parcellations are not associated with differences in the variance of parcel sizes (Supplementary Fig. 2). Second, we generate an ensemble of null FC matrices via the eigenstrapping method that randomizes fMRI data while preserving the spatial and temporal autocorrelation inherent in the data[78] (Supplementary Figs 3A–B; see 'Null FC matrices' in Methods). We find that the empirical H_{FC} of the geometric parcellations (Fig. 1E), and their performance relative to the existing benchmark parcellations (Supplementary Fig. 3C), are significantly higher than corresponding values observed in the null H_{FC} ensembles (see Supplementary Fig. 4 for replication with an alternative null model[79] described in Supplementary Information S2.2). These results indicate that it is the specific orientation and placement of the parcels of the geometric atlases, and not just low-level features such as the distribution of parcel sizes or the grid-like boundaries, that confers high functional homogeneity.

The grid-like structure of the geometric parcellations also arises in part from the use of a population-averaged cortical surface template, which smooths fine-scale anatomical variations and retains only coarse geometric features of the cortex. Applying our approach to individual cortical geometries yields regional borders that are more clearly aligned with the sulcal and gyral anatomy of individuals (Supplementary Fig. 5A; Supplementary Information S3) and yields regions with higher average H_{FC} than the template-based approach (Supplementary Fig. 5B) especially at coarse resolutions. Moreover, we find that the high homogeneity of individual parcellations is specific to an individual's FC data (Supplementary Fig. 5C), further supporting the specificity of the geometric effects captured by our approach. We nonetheless focus on template-based geometric parcellations in subsequent analyses because most of the brain phenotypes that we investigate to further validate our approach are not individual-specific (see also Supplementary Information S3).

Having established the high FC-based functional homogeneity of the geometric parcellations with respect to three independent datasets, we next evaluate parcel-level homogeneity across 242 diverse non-FC cortical phenotypes or maps drawn from open-source repositories[14,80,81] (Fig. 2A; see 'Brain phenotypes' in Methods for details). These maps include 1 morphometry map (cortical thickness); 3 microstructure maps (T1w:T2w ratio – an MRI metric that indirectly probes intracortical myeloarchitecture[82], NDI – neurite density index, and ODI – orientation dispersion index); 50 cytoarchitecture maps (layer-specific cell density); 5 metabolism maps derived from positron emission tomography (PET) (CMRGlu – cerebral metabolic rate of glucose, CBV – cerebral blood volume, CBF – cerebral blood flow, $CMRO_2$ – cerebral metabolic rate of oxygen, and synaptic density); 1 gene expression map (first principal component of gene profiles); 19 chemoarchitecture maps (i.e., neurotransmitter receptor density maps derived from PET); 47 HCP task-activation maps; and 116 meta-analytic task-activation maps from Neurosynth[81]. For each map, we estimate map-specific homogeneity, denoted H_{map}, as the inverse of the variance of map values across the vertices within a region (see 'Calculation of regional homogeneity' in Methods). Comparing H_{map} for different parcellations across such a diverse set of brain maps ensures that our findings cannot be attributed to the idiosyncrasies of any specific imaging modality (e.g., fMRI) or brain property (e.g., FC).

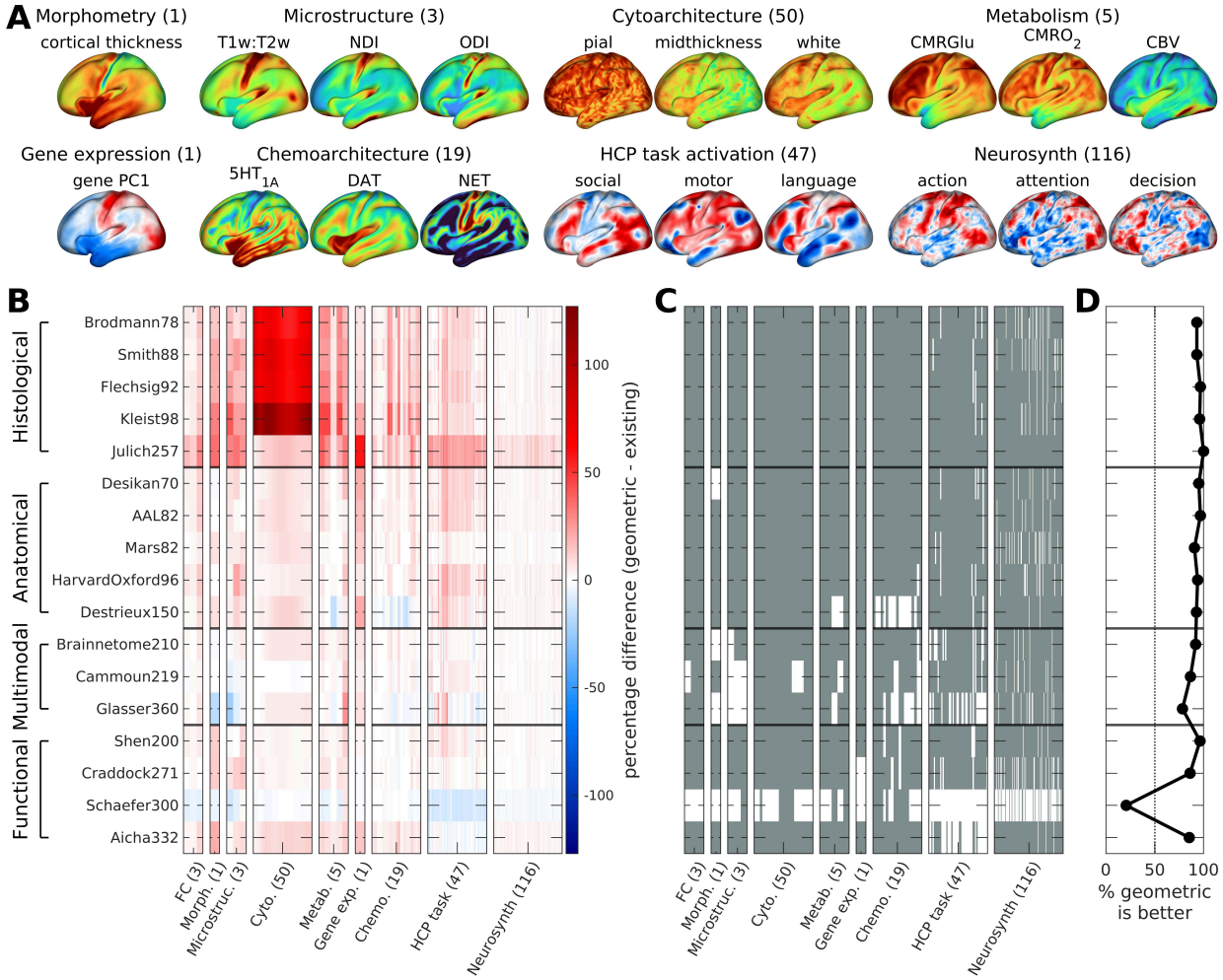

Fig. 2. Homogeneity of the geometric parcellations across diverse maps of the human neocortex. (**A**) Examples from 242 non-FC brain maps derived from various modalities capturing distinct phenotypes, including those related to morphometry, microstructure, cytoarchitecture, metabolism, gene expression, chemoarchitecture, HCP task activation, and Neurosynth task activations. The number beside the phenotype's group name denotes the total number of available maps. For phenotypes with more than three maps, only three representative maps are visually shown for brevity. (**B**) Percentage difference in the homogeneity of geometric parcellations relative to existing parcellations. Each row shows the result for one parcellation and each column shows the result for one brain map (including the three FC-based results in Fig. 1D), where red indicates superior performance for geometric parcellations. (**C**) Binarized version of panel B, where gray indicates superior or equivalent performance for geometric parcellations, with equivalence quantified as a difference threshold of ±1%. (**D**) Percentage of maps where the geometric parcellations have superior or equivalent performance relative to the existing parcellations.

Figures 2B–C show that the geometric parcellations consistently demonstrate superior performance, outperforming some existing parcellations in certain maps by more than 100%. More specifically, we find that the geometric parcellations have higher or equivalent homogeneity for >78% of the brain maps relative to 16 out of 17 benchmark parcellations (Fig. 2D; see Supplementary Fig. 6A for other equivalence thresholds). The exception is again the Schaefer300 atlas, which shows higher homogeneity than its geometric counterpart across 79.2% of the maps, highlighting the excellent generalizability of this FC-derived parcellation. However, the average performance difference between Schaefer300 and the corresponding geometric parcellation is

4.5% (min=1.0%, max=14.4%), which is small compared to, for example, the difference between geometric and histological parcellations, where the former show an average homogeneity advantage of 23.3% (min=1.0%, max=127%). These findings suggest that atlases derived from gold-standard cytoarchitecture and other histological techniques define parcels that lack generalizable homogeneity across multiple brain phenotypes.

Despite these comparisons, we emphasize that our goal here is not to identify a single 'optimum' parcellation for all applications, since the utility of an atlas will depend on the question under investigation (e.g., see ref.[83] for a systematic comparison of atlases). Instead, the strong performance of our simple approach, which requires only a model of the geometry of the cortex from a T1w anatomical scan, implies that it approximates the key features of a generative process that shapes a rough blueprint of cortical regional organization. The final boundaries of cortical areas may then be refined by experience-dependent and other processes, which may be somewhat better captured by the sophisticated FC-based clustering algorithm used to define the Schaefer300 atlas. Our results nonetheless demonstrate how a simple process, influenced only by geometry, is sufficient to delineate cortical regions with high functional, cellular, and molecular homogeneity.

Geometric constraints on cortical regionalization generalize to other mammals

We propose that the hierarchical geometric processes implicit in our parcellation method capture the essence of a highly conserved mechanism for defining the multiscale regional organization of the brain. We now test this conservation by investigating the generalizability of our approach to the neocortices of other non-human species; specifically, the macaque, marmoset, and mouse. For the macaque and marmoset, we apply the same algorithm used in Fig. 1A to a triangular mesh representation of their population-averaged cortical surfaces (10,242 vertices for each hemisphere of the macaque; 37,974 and 38,094 for the left and right hemispheres of the marmoset, respectively). For the mouse, we apply the algorithm to its neocortex in three-dimensional (3D) volumetric space (200 μm isotropic voxel resolution; see 'Derivation of geometric eigenmodes' in Methods) because existing atlases of the mouse brain are only available in volumetric space.

We benchmark the performance of our geometric approach against 15 existing parcellations derived from histological and multimodal data (Fig. 3A; Supplementary Table 1) and 114 different cortical phenotypes available across the three species (10, 4, and 1 parcellations and 20, 5, and 89 phenotypes for the macaque, marmoset, and mouse, respectively). The phenotypes are related to resting-state FC (measured using fMRI and calcium imaging), morphometry, microstructure, chemoarchitecture, cytoarchitecture, and gene expression (see 'Benchmark brain parcellations' and 'Brain phenotypes' in Methods for details). Once again, our use of both *in vivo* and *ex vivo* data spanning functional, cellular, and molecular properties across all the three species ensures that our findings cannot be attributed to the specific details of any specific measurement modality or brain property.

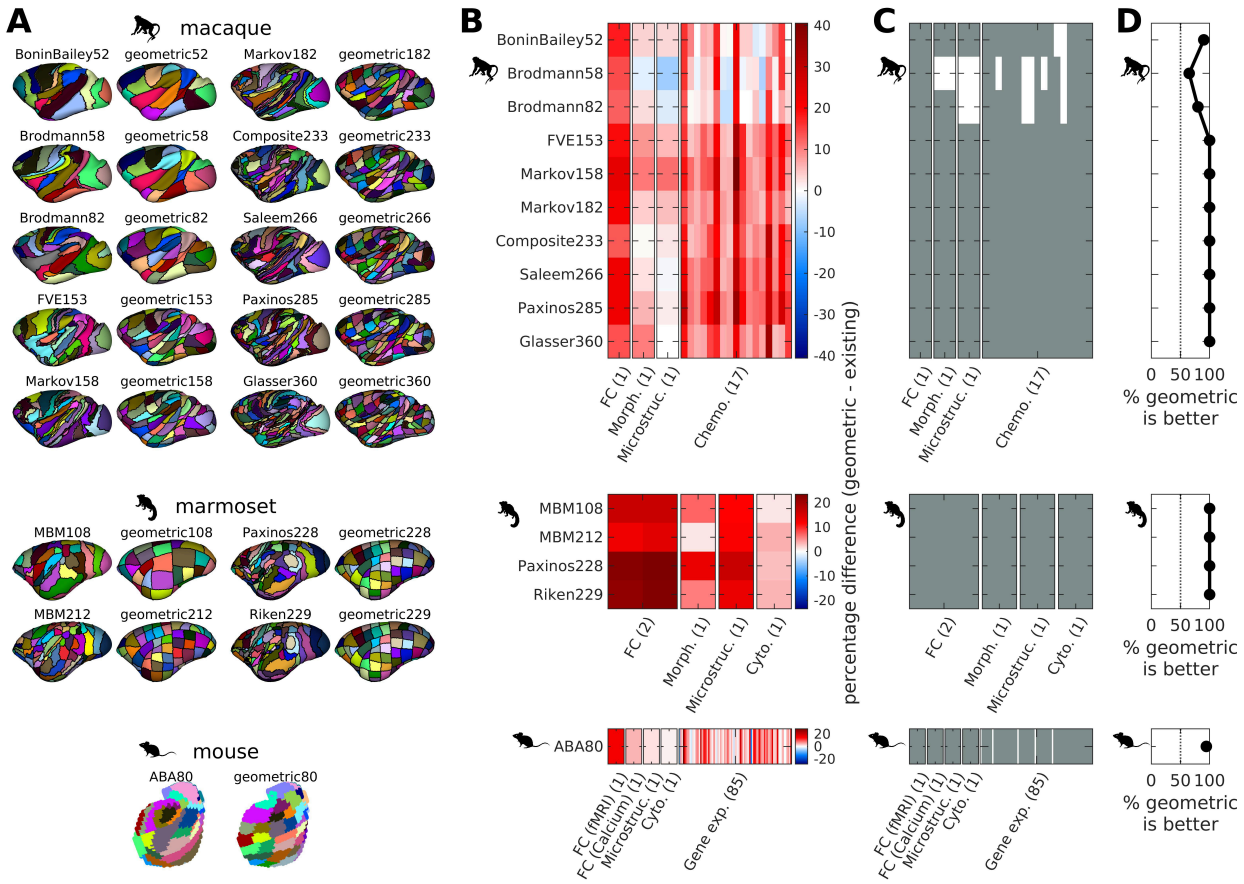

Fig. 3. Geometric parcellations of the macaque, marmoset, and mouse neocortex. (**A**) Existing benchmark parcellations and corresponding geometric parcellations with matched number of parcels. The number beside the parcellation's name denotes the total number of parcels across both hemispheres. (**B**) Percentage difference in the homogeneity of geometric parcellations relative to existing parcellations. Each row shows the result for one parcellation and each column shows the result for one brain map, where red indicates superior performance for geometric parcellations. (**C**) Binarized version of panel B, where gray indicates superior or equivalent performance for geometric parcellations, with equivalence quantified as a difference threshold of ±1%. For panels B and C, the number beside the phenotype's group name denotes the total number of available maps. (**D**) Percentage of maps where the geometric parcellations have superior or equivalent performance relative to the existing parcellations.

Figures 3B–C show that our geometric parcellations again consistently demonstrate superior performance relative to existing parcellations. Specifically, we find that the geometric parcellations have higher or equivalent homogeneity for >65%, 100%, and 94.4% of the brain phenotypes in the macaque, marmoset, and mouse, respectively (Fig. 3D; see Supplementary Figs 6B–D for other equivalence thresholds). In the macaque, the only instances in which our geometric parcellation show lower homogeneity are relative to BoninBailey52, Brodmann58, and Brodmann82 parcellations in 2, 7, and 4 out of 20 maps, respectively. Notably, these parcellations only outperform the geometric parcellations by an average of 3.5% (min=1.2%, max=7.4%). This value is small compared to the 12.6%, 14.3%, and 18.0% higher FC homogeneity of the geometric parcellations relative to the BoninBailey52, Brodmann58, and Brodmann82 atlases, respectively. In the mouse, the ABA80 atlas only outperforms the geometric parcellations in 5 out of 89 maps (all related to gene expression) by an average of 5.4% (min=1.8%, max=12.8%).

The strong performance of the geometric approach is notable given that many of the non-human primate and mouse parcellations have been defined through careful cytoarchitectonic analysis, which is often considered the gold standard in the field. As suggested by the analysis of the human data, our results in these animals indicate that such parcellations may only characterize one specific aspect of organization at a particular spatial scale that may not generalize to other properties of cortical organization. Conversely, the consistently strong performance of the geometric parcellations further supports the universality of our approach in defining homogeneous parcels at any arbitrary resolution for any species.

A key advantage of our approach is that it is simple, fast, and flexible, requiring only a geometric model of a given brain structure, which can easily be obtained from T1w MRI. This simplicity contrasts with classical approaches that require expensive and time-consuming manual investigation of regional cytoarchitecture or the application of sophisticated cluster analyses to high-dimensional physiological data. The simplicity and generality of our algorithm means that it can easily be applied to generate a reasonable first approximation of the regional organization of species that have not been extensively studied and for which no parcellations exist.

To further demonstrate the flexibility of our approach, we use an open-source repository of cortical surfaces of 24 various species from the Euarchontoglires superorder of mammals (also known as Supraprimates), which includes the groups of Primata, Scandentia, Dermoptera, Rodentia, and Lagomorpha[84]. Figure 4 shows that we can successfully produce geometric parcellations for any species at any arbitrary resolution within the spatial limits of MRI (the example panels show 8, 16, and 32 parcels). These new parcellations open new opportunities to study the regional properties of the brains of these mammalian species that would not otherwise be possible. We provide this library of parcellations as an open resource to facilitate future comparative research and validation (see 'Data availability' section).

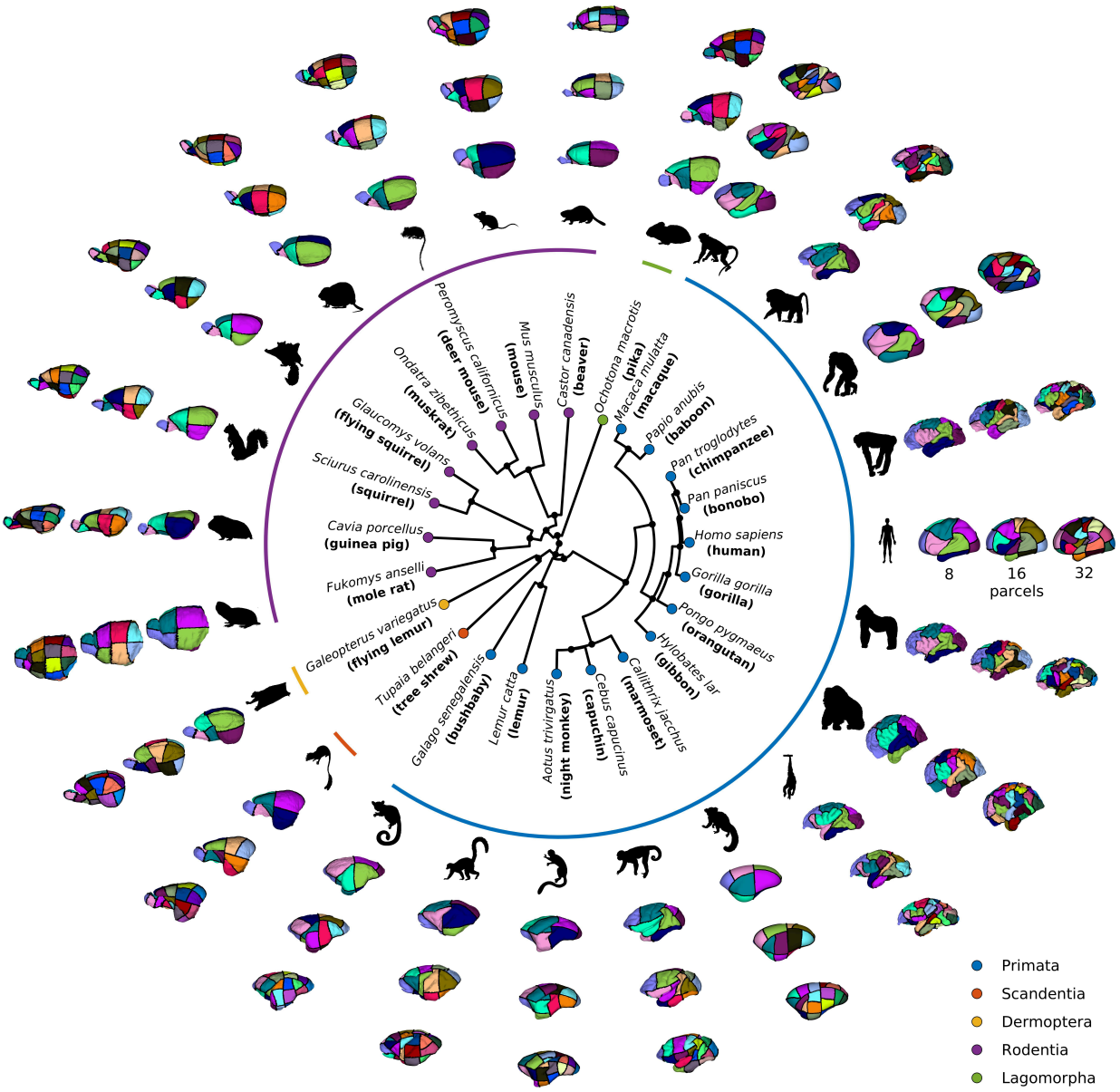

Fig. 4. Geometric parcellations of 24 diverse mammalian species. The center graph shows the phylogenetic relationships between the species from 5 groups of the Euarchontoglires mammalian superorder[84]; i.e., Primata, Scandentia, Dermoptera, Rodentia, and Lagomorpha. For each species, the insets show their example geometric parcellations with 8, 16, and 32 parcels (from inner to outer ring).

Geometric constraints on regionalization generalize to non-neocortical structures

Having demonstrated the generality of our approach for characterizing the regionalization of the cortex of diverse species, we next consider how geometry shapes the multiscale regionalization of non-neocortical (i.e., subcortical and allocortical) structures of the human brain, focusing on the following 7 structures: hippocampus (HIP); amygdala (AMY); thalamus (THA); nucleus accumbens (NAc); globus pallidus (GP); putamen (PUT); and caudate (CAU). We generate geometric parcellations specific to each of these 7 structures using 3D volumetric (voxel-based) models of their geometry derived from T1w MRI (at 2 mm isotropic voxel resolution)[58]. We then evaluate the performance of the geometric parcellations against 20 existing benchmark

parcellations across the 7 structures (Fig. 5A; Supplementary Table 2; specifically 4, 2, 6, 2, 2, 2, and 2 parcellations for HIP, AMY, THA, NAc, GP, PUT, and CAU, respectively) in the three independent resting-state fMRI FC datasets analyzed in Fig. 1 (i.e., HCP, GSP, and Monash). These benchmark parcellations were derived using a variety of approaches based on cytoarchitecture, myeloarchitecture, resting-state fMRI, and diffusion MRI (Supplementary Table 2).

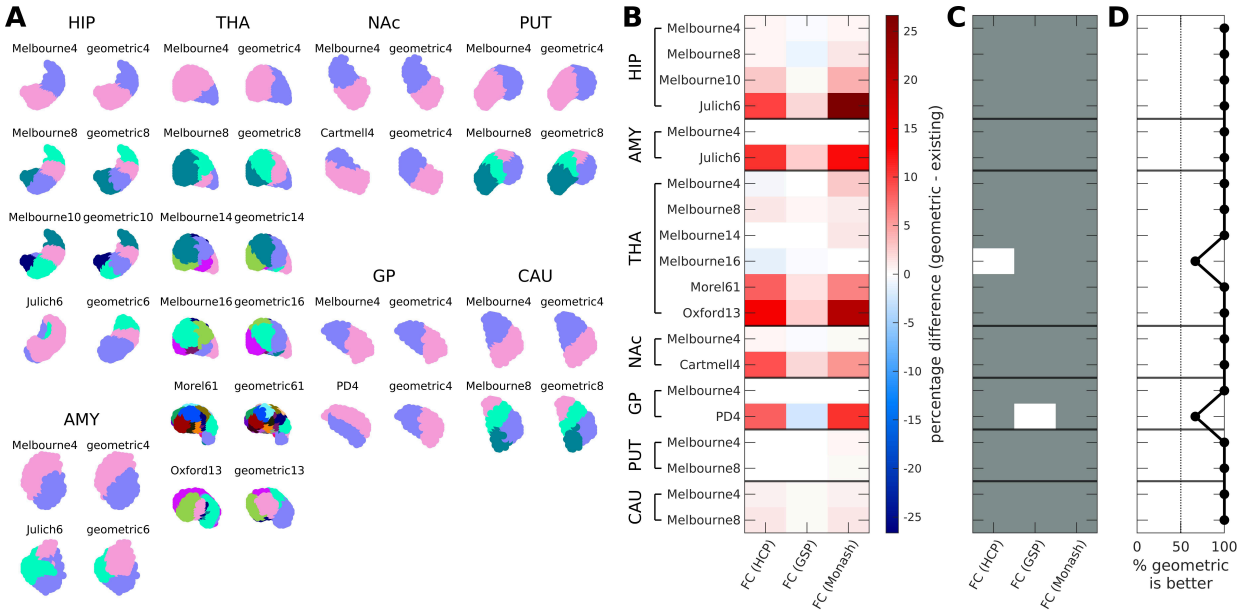

Fig. 5. Geometric parcellations of 7 human non-neocortical structures. (**A**) Existing benchmark parcellations and corresponding geometric parcellations with matched number of parcels across the 7 structures (HIP: hippocampus; AMY: amygdala; THA: thalamus; NAc: nucleus accumbens; GP: globus pallidus; PUT: putamen; CAU: caudate). The number beside the parcellation's name denotes the total number of parcels across both hemispheres. (**B**) Percentage difference in the homogeneity of geometric parcellations relative to existing parcellations. Each row shows the result for one parcellation and each column shows the result for one FC dataset, where red indicates superior performance for geometric parcellations. (**C**) Binarized version of panel B, where gray indicates superior or equivalent performance for geometric parcellations, with equivalence quantified as a difference threshold of ±1%. (**D**) Percentage of maps where the geometric parcellations have superior or equivalent performance relative to the existing parcellations.

Figures 5B–D show that the geometric parcellations of the 7 human non-neocortical structures consistently show higher or equivalent H_{FC} relative to existing parcellations. The only exception is the comparison with the Melbourne16 THA parcellation on the HCP dataset and the PD4 GP parcellation on the GSP dataset, where the homogeneity difference is 1.1% and 2.1%, respectively (slightly above our homogeneity equivalence threshold of 1%; see Supplementary Fig. 6E for other thresholds). Moreover, the geometric parcellations across different scales strongly correspond to the boundaries defined by many of the existing parcellations, particularly those of the Melbourne4 parcellations for HIP, AMY, NAc, GP, PUT, and CAU (average Dice coefficients of 0.93, 0.94, 0.95, 0.97, 0.93, and 0.94, respectively). This is because the Melbourne parcellations draw regional boundaries based on sharp transitions in spatially varying FC gradients, which correspond almost precisely with the geometric eigenmodes of these non-neocortical structures[58]. Our geometric approach thus achieves a similar result without the need for data-intensive analyses of fMRI data.

Together, these findings further underscore the universality of geometric constraints on the regional organization of different brain structures.

Hierarchical geometric parcellation mimics a sequential reaction-diffusion process

Our geometric algorithm rests on an implicit generative model of the brain's regional organization that emphasizes two principal mechanisms: (1) the fundamental physical constraints imposed by geometry on the diffusion of early patterning molecules; and (2) recursive bipartition to generate a hierarchical, multiscale architecture. Here, we demonstrate how these two mechanisms capture the essence of a generic reaction-diffusion process hypothesized to play a role in establishing a multiscale map of regional organization in the developing brain.

For brevity, we focus on the human neocortex and simulate a linearized reaction-diffusion (RD) model of an activator-inhibitor type[60] (see 'Reaction-diffusion model' in Methods). We emphasize that our model is not intended to precisely capture the actions of any specific molecule or interactions between a set of molecules, as their biophysical details are often unknown (for exceptions, see refs[85,86]). The model instead identifies a minimally sufficient set of physiological mechanisms that can yield the regional patterning implied by our geometric parcellation algorithm.

We first focus on molecules seeded at maximally distant points near the rostral and caudal poles of the left hemisphere (Fig. 6A), following evidence that several morphogens and transcription factors (e.g., *Emx2* and *Pax6*) show opposing concentration gradients along the rostrocaudal (RC) axis[50,56]. Depending on model parameter combinations, Turing has shown that our type of model can lead to the spontaneous emergence of spatially non-constant solutions, via what is termed a spatial Turing instability[41] (see 'Reaction-diffusion model' in Methods for the instability conditions). Figure 6B (top row) shows the equilibrium RD solution for $(u - v)$ using the seeds in Fig. 6A and parameters that induce a Turing instability (see 'Reaction-diffusion model' in Methods for the specific parameters). The model RD solution gives rise to an increase of u and v in separate halves of the cortex ($u > v$ in one half towards the rostral pole and $v > u$ in the other half towards the caudal pole), partitioning the cortex into two subregions separated by a nodal line that bears a striking qualitative resemblance to the RC eigenmode (Fig. 6B bottom row)—the starting point of our parcellation algorithm (Fig. 1A). The high similarity of the model RD solution and RC eigenmode and their corresponding parcellations are quantitatively evidenced by a high spatial correlation (0.85) and ahigh Dice coefficient (0.82). Note that the spatial pattern of the model RD solution in Fig. 6B is robust and can be reproduced when the linear activator-inhibitor interactions in the model are changed to nonlinear functions (Supplementary Fig. 7).

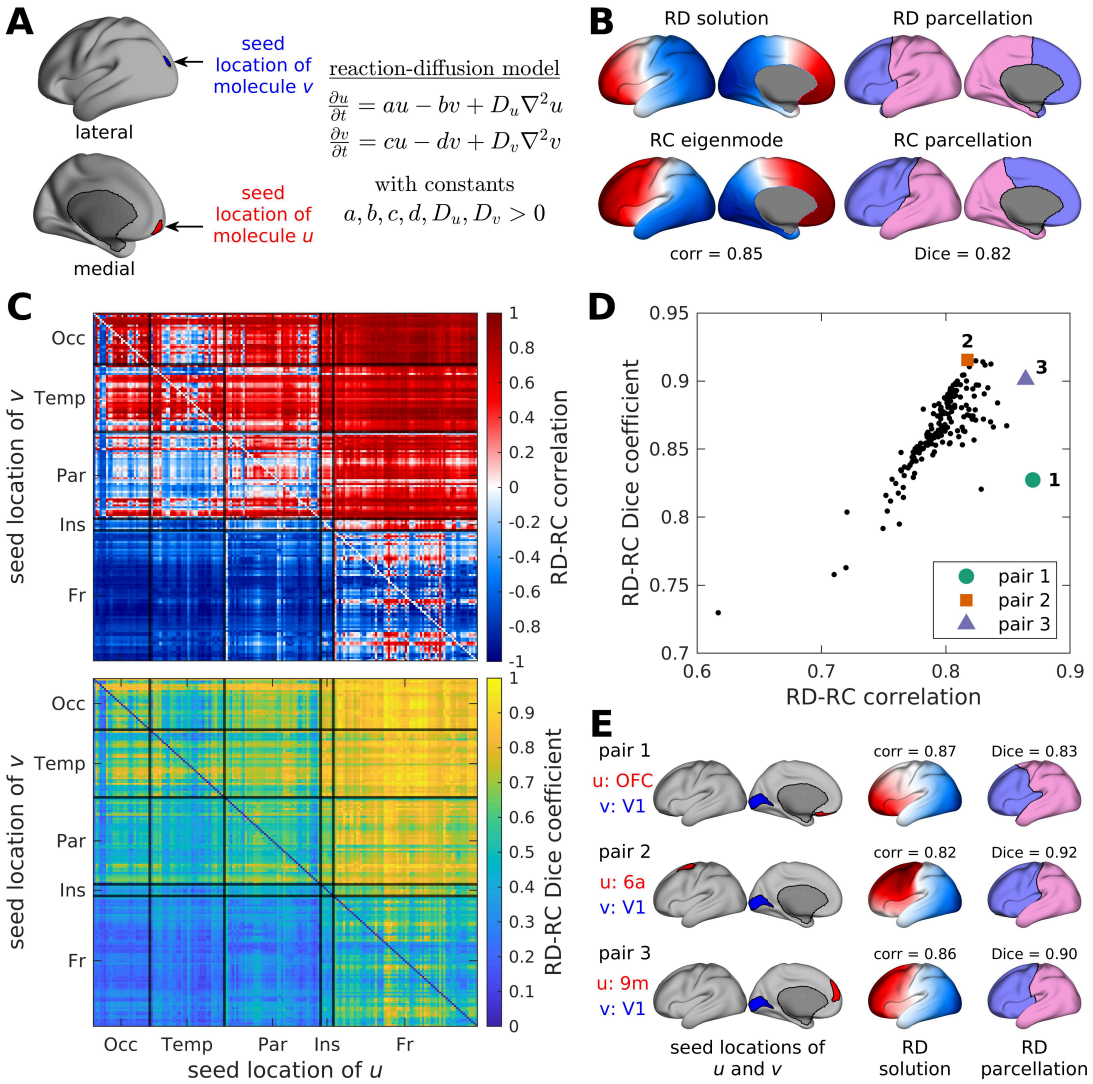

Fig. 6. Model-based parcellation via a reaction-diffusion process. (**A**) We use a reaction-diffusion model that assumes two molecules, u and v, are seeded from distinct locations and diffuse in space and time with diffusion constants D_u and D_v, respectively. The schematic shows example seed locations of the molecules at maximally distant points near the rostral and caudal poles of the left hemisphere, specifically at regions 10pp (orbital prefrontal cortex) and V3B for u and v, respectively, based on the Glasser360 parcellation[2]. The constants a, b, c, and d are assumed to be positive, such that the interaction assigns molecule u to be the activator and molecule v to be the inhibitor. (**B**) The top row shows an example model reaction-diffusion (RD) solution ($u - v$) and parcellation using parameter combinations that induce a Turing spatial instability. The instability conditions are: $D_u < D_v$; $a < d$; $ad < bc$; and $d/D_v < a/D_u$. The molecules are seeded at the locations described in panel A. The bottom row shows the rostrocaudal (RC) geometric eigenmode and parcellation. Correspondences between the model RD solution and RC eigenmode and their respective parcellations are quantitatively shown in terms of spatial correlation and Dice coefficient, respectively. (**C**) The two matrices show the spatial correlation of the model RD solutions and the RC geometric eigenmode (top matrix) and the Dice coefficients of their resulting parcellations (bottom matrix) when molecules u and v are seeded in various locations. Each location is assigned to one of five anatomical cortices: Occipital (Occ); Temporal (Temp); Parietal (Par); Insular (Ins); and Frontal (Fr). Correlations remain high as long as the activator u is seeded anywhere in the front of the brain and the inhibitor v is seeded anywhere in the back of the brain. (**D**) RD-RC spatial correlation and Dice coefficient when the inhibitor v is seeded at V1 and the activator u is seeded anywhere. Each point represents a different seed location for u. Three pairs of the molecules' seed locations are highlighted that either provide high spatial correlation, high Dice coefficient, or both. (**E**) Seed locations of the molecules, resulting model RD solution, and resulting RD parcellation (from left to right) of the three pairs highlighted in panel D.

Figure 6C shows the effect of seeding molecules u and v at different locations using the parameter combinations that produce the RD solution in Fig. 6B. The correspondence between the model RD solution and RC geometric eigenmode, and their resulting parcellations, is extremely robust, with high spatial correlations (mean=0.75, median=0.79, min=–0.07, max=0.99) and high Dice coefficients (mean=0.84, median=0.85, min=0.48, max=0.98) obtained as long as the activator molecule u is seeded anywhere in the frontal cortex and the inhibitor molecule v is seeded anywhere in the occipital or temporal cortices.

Some of the most robust correspondences between the model RD solution and RC geometric and their respective parcellations are obtained when the inhibitor molecule v is seeded at region V1 (primary visual cortex) regardless of the seed location of the activator molecule u, with mean spatial correlation of 0.80 (min=0.62, max=0.87) and mean Dice coefficient of 0.86 (min=0.73, max=0.92) as shown in Fig. 6D. This result is notable given that V1 is the most cytoarchitectonically and transcriptomically distinct region of the primate neocortex[45,87,88] and is the last such region to complete neurogenesis[89]. Figure 6E shows specific optimal solutions with either high spatial correlation, high Dice coefficient, or both when the activator molecule u is seeded at regions OFC (orbitofrontal cortex), 6a (premotor cortex), and 9m (anterior part of the dorsomedial prefrontal cortex), respectively. This robustness supports a consistent geometrically constrained blueprint for regional patterning in the face of biological noise[90].

In principle, the RD model can be iterated to generate recursive divisions within each partition to obtain a parcellation at any given scale that will strongly resemble the results of our purely geometric approach. The model thus implies that spatial variations in molecular concentrations defined by the equilibrium solutions of the RD process represent thresholds for triggering the diffusion of other molecules and more finely-tuned cellular and molecular processes within each subdomain or partition. This process echoes the threshold-dependent molecular dynamics proposed in Wolpert's classical model of the French Flag problem, which aims to understand how positional information is conferred upon developing cellular arrays[91,92]. Our model implies that the new molecule distributions further destabilize along the dominant geometric eigenmode of each subregion to yield another division into two new subregions. In this way, the recursive bipartitions of our geometric algorithm can be understood as a hierarchical sequence of Turing instabilities, with each stage triggering the next set of reaction-diffusion processes that is very robust to the specific parameterization and details of the model (see Supplementary Information S1 for details). Indeed, our hierarchical geometric parcellation hypothesizes that once concentration levels saturate following the first division, a second instability is triggered within each of the two subregions that leads to further two-fold divisions of the subregions. Following this process, we would only need $\log_2 N$ hierarchical levels to produce N regions, which is efficient and biologically feasible (see Supplementary Information S1.4). A similar mechanism of threshold-dependent cascading is thought to underlie the progressive segmentation of the *Drosophila* body plan along the RC axis[93,94]. This recursive process may thus capture a conserved aspect of regional patterning that supports the progressive compartmentalization of different structures[65,68,95], which can be effectively approximated by the first non-constant geometric eigenmode (i.e., the RC eigenmode at the first division). Accordingly, this eigenmode strongly aligns with a highly conserved gradient of neurogenic timing and neuronal density in mammals[96,97].

Conclusions

An accurate understanding of the regional organization of the mammalian brain is essential for comprehending the functional specialization of distinct brain regions, and is fundamental for models that characterize how these specialized functions are integrated to support coordinated behavior[4,5]. Distinct regions of the brain have traditionally been defined using descriptive approaches that are agnostic to how the regions arise in the first place. Here, we have developed a generative approach to brain parcellation that relies on a simple, hierarchical, and geometrically constrained process to derive a regional parcellation of the brain at any given resolution scale. We have shown that this approach defines regions in both neocortical and non-neocortical structures with greater functional, cellular, and molecular homogeneity than those in almost all existing, popular benchmark parcellations in humans, macaques, marmosets, and mice brains. Critically, we have demonstrated that the simplicity of our approach, which only requires a model of brain geometry as input (e.g., from T1w MRI), allows it to be generalized to any brain structure in any mammalian species to create a parcellation of any arbitrary resolution within seconds. We further demonstrate that our approach mimics a sequential reaction-diffusion process that may represent a conserved developmental mechanism for establishing a multiscale map of regional organization in the mammalian brain.

We emphasize that while a reaction-diffusion mechanism has extensive biological applicability[85,86,98], the mechanism itself and the hierarchical approach we propose are approximations and exclude more complex molecular interactions. For instance, some aspects of areal patterning do not need two interacting morphogens[99,100] and patterning gradients that predominantly run along the non-rostrocaudal axes of the brain (at the first division) have also been identified[51]. Future work could extend our approach to account for these higher-order influences, in addition to the role of thalamocortical afferents, which are likely to perturb the initial organization established by our recursive geometric procedure, interacting with postnatal brain growth and activity-dependent processes to refine areal boundaries[51]. Nonetheless, the striking performance of our method demonstrates that a simple, neurodevelopmentally-inspired hierarchical process anchored by the dominant geometric eigenmode is minimally sufficient to create a robust and highly generalized blueprint of areal organization, offering a unified approach to study the multiscale regional organization of any mammalian brain structure. Its flexibility for use in species for which no parcellations exist offers immediate practical and neuroscientific advantages for comparative research. The strong performance of our approach, observed across diverse anatomical, cellular, molecular, and functional properties, points to a fundamental role of geometry in shaping the regional organization of the mammalian brain.

Methods

Geometry of neocortical and non-neocortical structures

The only input to our geometric parcellation approach is a T1w magnetic resonance imaging (MRI)-derived representation of a brain structure's geometry either at the vertex level (for surfaces) or voxel level (for volumes). For the human neocortex, we used the fsaverage template of its midthickness surface[101], resampled in fsLR_32k space with 32,492 vertices for each hemisphere. For the macaque neocortex, we used the Yerkes19 template of its midthickness surface[102], resampled in fsLR_10k space with 10,242 vertices for each hemisphere. For the marmoset neocortex, we used the Marmoset Brain Mapping v3 (MBMv3) template of its

565 midthickness surface[103], resampled in fsaverage_38k space with 37,974 and 38,094 vertices for
566 the left and right hemispheres, respectively. For the mouse neocortex, we used the Allen Mouse
567 Brain Common Coordinate Framework v3 (CCFv3) template in three-dimensional (3D)
568 volumetric space at 200 μm isotropic voxel resolution.

569 For the 24 Euarchontoglires mammalian species, we used reconstructions of their cortical surfaces
570 in fsaverage6 space with 40,962 vertices for each hemisphere[84]. Phylogenetically, the 24 species
571 belong to 5 groups; i.e., Primata, Scandentia, Dermoptera, Rodentia, and Lagomorpha. The
572 Primata group comprises 13 species: *Macaca mulatta* (macaque); *Papio anubis* (baboon), *Pan*
573 *troglodytes* (chimpanzee); *Pan paniscus* (bonobo); *Homo sapiens* (human); *Gorilla gorilla*
574 (gorilla); *Pongo pygmaeus* (orangutan); *Hylobates lar* (gibbon); *Callithrix jacchus* (marmoset);
575 *Cebus cappuchinus* (capuchin); *Aotus trivirgatus* (night monkey); *Lemur catta* (lemur); and
576 *Galago senegalensis* (bushbaby). The Scandentia group comprises 1 species: *Tupaia belangeri*
577 (tree shrew). The Dermoptera group comprises 1 species: *Galeopterus variegatus* (flying lemur).
578 The Rodentia group comprises 8 species: *Fukomys anselli* (mole rat); *Cavia porcellus* (guinea pig);
579 *Sciurus carolinensis* (squirrel); *Glaucomys volans* (flying squirrel); *Ondata zibethicus* (muskrat);
580 *Peromyscus californicus* (deer mouse); *Mus musculus* (mouse); and *Castor canadensis* (beaver).
581 The Lagomorpha group comprises 1 species: *Ochotona macrotis* (pika).

582 For the human non-neocortical structures, we converted the existing parcellations of the 7
583 structures, i.e., hippocampus (HIP), amygdala (AMY), thalamus (THA), nucleus accumbens
584 (NAc), globus pallidus (GP), putamen (PUT), and caudate (CAU), into volumetric binary masks
585 in the Montreal Neurological Institute (MNI) space at 2 mm isotropic voxel resolution. This is to
586 ensure that the coverage and number of voxels in the geometric parcellations match those of the
587 existing parcellations for fair comparison. Further details of the existing non-neocortical
588 parcellations are described in the 'Benchmark brain parcellations' section.

589

590 **Derivation of geometric eigenmodes**

591 Our parcellation method uses the geometric eigenmodes of the brain to delineate regional
592 boundaries. The eigenmodes are obtained by solving the Helmholtz equation defined in Eq. (1) of
593 the main text. The Laplace-Beltrami operator (LBO) in Eq. (1) captures the intrinsic geometry of
594 the brain structure of interest (e.g., cortical surface), i.e., geometric and spatial relations between
595 mesh vertices[104], and is defined generally as[105],

596

597 $$\Delta \coloneqq \frac{1}{W}\sum_{i,j}\frac{\partial}{\partial x_i}\left(g^{ij}W\frac{\partial}{\partial x_j}\right), \tag{2}$$

598

599 where x_i, x_j are the local coordinates, $(g^{ij}) \coloneqq G^{-1}$ with G being the matrix of inner product of
600 metric tensors $g_{ij} \coloneqq \langle\frac{\partial}{\partial x_i}, \frac{\partial}{\partial x_j}\rangle$, $W \coloneqq \sqrt{\det G}$, and det denotes the determinant. For surfaces, such
601 as the human, macaque, and marmoset neocortices, we constructed the LBO using a triangular
602 mesh representation of the T1w MRI-derived cortical sheet. For solid 3D structures, such as the
603 mouse neocortex and human non-neocortical structures, we converted their T1w MRI-derived
604 volumetric binary masks into tetrahedral meshes to account for the full 3D geometry of the
605 structures (see ref.[58] for further details). Note, however, that the LBO can also be constructed using

a model of a brain structure's geometry derived from alternative methods (e.g., microscopy) and is not restricted to T1w MRI.

To numerically calculate the geometric eigenmodes, we used our previously published code[58] based on the LaPy Python library[104,106] installed on the MASSIVE High Performance Computing facility[107]. The eigenvalue solutions of the Helmholtz equation in Eq. (1) are ordered sequentially according to the spatial wavelength of the spatial patterns of each eigenmode; i.e., $0 \leq \lambda_1 \leq \lambda_2 \leq \cdots$. Note that the first eigenvalue λ_1 is approximately equal to zero (wavelength $\gg$ size of the brain) and the corresponding eigenmode ψ_1 is a constant function with no nodal lines (zero sets of the function). Low-order eigenmodes 2, 3, and 4 correspond to spatial patterns with one nodal line and have antinodes at the opposing ends of the rostrocaudal, dorsoventral, and mediolateral axes, respectively. We further note that while our work is inspired by processes governing the developing brain, we only analyzed the adult brain because low-order eigenmodes of both the developing and adult brain are largely invariant[108]. Future work may consider the impact of cortical growth on the reaction-diffusion mechanisms that we model here[109,110].

Hierarchical partitioning

Our geometric approach uses the nodal lines of the eigenmodes to partition a brain structure into subregions. Specifically, we use only the first non-constant eigenmode ψ_2, which is the most dominant axis of variation along the rostrocaudal direction at the first division, to partition the structure into two subregions of approximately equal sizes. Although models of regional patterning based on gradients aligned with other axes have been proposed[111], we focus only on the first non-constant geometric eigenmode based on physical principles related to Turing instabilities to identify the simplest possible mechanism through which a regional parcellation of the brain may be obtained (see Supplementary Information S1). Other instabilities (with a shorter wavelength) are more stable and cannot occur first.

We applied the bipartitioning in an iterative, hierarchical manner, calculating the first non-constant geometric eigenmode of each subregion and using it to further subdivide the subregion. By construction, performing N iterations will yield a parcellation with 2^N parcels. However, the multiscale organization of the brain means that the optimal number of regions to define remains unclear. Hence, we generalized the approach across scales, such that one can set the number of regions to an arbitrary number between 1 and 2^N. We do this by constructing a tree of eigenvalues from each iteration of the approach. We performed a maximum of 9 iterations to reduce computational burden (Supplementary Fig. 1A). We followed the tree of division from the first to N iterations, tracking the parent and daughter subdivisions and arranging them according to the magnitude of the eigenvalues of their first non-constant geometric eigenmodes. The lower the eigenvalue is, the more dominant that subdivision is. Hence, to generate a parcellation with $m > 1$ regions, we retained the subdivisions corresponding to the first $m - 1$ smallest eigenvalues. To ensure that the intrinsic uniformity of the region sizes of the geometric parcellation (Supplementary Figs 1C–D) is maintained, we additionally constrained the method by choosing all subdivisions within an iteration first before moving to the subdivisions of the subsequent iteration. We performed this process to separately parcellate the left and right hemispheres.

The strength of our hierarchical approach is that it affords a multiscale insight into the brain's regional organization. Parcellations can thus be tailored to the problem of interest, unlike the multitude of brain atlases available for use today that are only defined at a single resolution scale and thus ignore the intrinsically hierarchical organization of the brain. For instance,

cytoarchitectonic studies clearly differentiate primary sensory areas such as V1 and S1 from adjacent regions, but it is still possible to identify further functional subdivisions within these borders, such as areas processing sensory information from distinct body regions within S1 or distinct, overlapping modes of functional organization within V1[34]. The correspondence between such subregional organization and the areas defined by our approach remains to be explored, but our method nonetheless allows one to test hypotheses about how such nested functional organization may arise.

Our hierarchical bipartitioning approach mimics the processes that shape the embryonic development of various hierarchically arranged organs such as limbs, digits and vascular trees[60,62–66,112]. A bipartitioning process is favored by nature because it provides subdivisions that are robust, reliable, and insensitive to the size of the domain[65]. Hence, dividing domains of different sizes (e.g., human vs marmoset brains) into two subdomains one step at a time ensures that the subdomains will be relatively uniform in size compared to dividing the domains into several regions at once. This is important because high patterning precision is needed for robust development of brain organization (e.g., regions should generally be located in the same spatial location across individuals of a species)[90]. An interesting avenue of further work could investigate whether the regional organization of different brain areas is dictated by varying degrees of hierarchical depth in this recursive process.

Calculation of regional homogeneity

We compared the degree to which the geometric parcellations accurately capture the organization of the brain relative to existing benchmark parcellations (see 'Benchmark brain parcellations' section), with accuracy quantified in terms of parcel homogeneity. We assume that a parcel's boundary is likely accurate if the vertices or voxels enclosed by the parcel are homogeneous in some way. This homogeneity is commonly defined in relation to inter-vertex or inter-voxel functional coupling (FC)[12,70–73] (i.e., accurate parcels are those that define sets of vertices or voxels that show high internal FC with each other), but we go beyond this common practice by additionally measuring homogeneity in terms of more diverse brain phenotypes or maps related to morphometry, microstructure, cytoarchitecture, metabolism, gene expression, chemoarchitecture, and task-related functional architecture (see 'Brain phenotypes' section). This is to avoid reliance on one single measure or imaging modality and to provide a comprehensive validation of the geometric parcellations across diverse aspects of brain structure and function.

Note that recent work has proposed a different metric to compare the performance of brain parcellations[113], but it is most suitable only for functional data (e.g., resting-state and task-based fMRI), relies on an *a priori* choice of various heuristics (e.g., spatial bin size and weighted averaging scheme), and requires certain conditions in the data to be satisfied that are not always guaranteed (e.g., stability of within- and between-vertex correlations of functional profiles). Hence, we decided to use homogeneity (described below) to have a single, simple metric that can be generalized across diverse brain phenotypes or maps.

For each parcellation (geometric or existing), we calculated the overall parcellation homogeneity, H, as per prior work[72,76], as a weighted average,

$$H = \frac{\sum_{i=1}^{n} S_i P_i}{\sum_{i=1}^{n} S_i}, \tag{3}$$

where n is the total number of parcels across both hemispheres, S_i is the size of parcel i (i.e., total number of vertices or voxels enclosed by the parcel), and P_i is the summary statistic for parcel i calculated from the phenotype or map of interest. For resting-state FC, P_i is the average FC between all pairs of vertices or voxels within the parcel, such that a higher P_i means that the parcel is highly homogeneous. For non-FC spatial maps, P_i is the variance of map values across all vertices or voxels within the parcel, such that a lower P_i means that the parcel is highly homogeneous. We used a weighted average in Eq. (3) to take into account the fact that parcels with larger sizes will tend to have lower homogeneity (Supplementary Fig. 8A), following previous work[12,72], and to reduce the gyral and sulcal bias prevalent in cortical surface reconstructions[114]. The weighted average effectively decreases and increases the contribution of small and large parcels, respectively (Supplementary Fig. 8B). We pooled all P_i values from both the left and right hemispheres to calculate a whole-brain homogeneity value, except for cases in which maps were only available in one hemisphere.

We then compared the homogeneity of the geometric and existing parcellations ($H^{\text{geometric}}$ vs H^{existing}) as a percentage difference,

$$\delta H = 100 \times \left(\frac{H^{\text{geometric}} - H^{\text{existing}}}{H^{\text{existing}}} \right). \tag{4}$$

For non-FC maps, we took the inverse of H in Eq. (3) before substituting in Eq. (4) to ensure that $\delta H > 0$ consistently means that the geometric parcellation is more homogeneous than the existing parcellation.

Benchmark brain parcellations

We compared the homogeneity of our geometric parcellations to several existing benchmark parcellations of the human, macaque, marmoset, and mouse neocortices (Supplementary Table 1) and human non-neocortical structures (Supplementary Table 2). These were chosen because they are among the most used in the field and they were derived using diverse approaches and measures, including expert delineation and/or data-driven analysis of histological and/or imaging data (see references in the last column of Supplementary Tables 1–2). This diversity allows us to comprehensively assess the quality of the geometric parcellations. For each existing parcellation, we constructed a geometric parcellation specific to the left and right hemispheres with matched number of parcels (see the third column of Supplementary Tables 1–2) to ensure fair comparison.

Most of the parcellations were obtained directly from the references in the last column of Supplementary Tables 1–2, with some exceptions. Histological parcellations of the human neocortex (i.e., Brodmann78, Smith88, Flechsig92, and Kleist98) corresponded to the reconstructed versions in MNI space provided by ref.[115]. Parcellations of the macaque cortex (i.e., BoninBailey52, Brodmann58, FVE153, Markov158, Markov182, Composite233, and Paxinos285) were obtained from ref.[116]. All parcellations of the marmoset neocortex were obtained from the Marmoset Brain Mapping Project (https://marmosetbrainmapping.org/). All parcellations of the human non-neocortical structures, except the Melbourne parcellations, were obtained from https://www.lead-dbs.org. The Melbourne parcellations were obtained from https://github.com/yetianmed/subcortex. Finally, parcellations of the human, macaque, and

marmoset neocortices originally defined in volume space were projected onto surface space using the volume-to-surface-mapping command of the Connectome Workbench software. Small parcels with less than 20 vertices were removed because they may have resulted from inaccuracies in the volume-to-surface projection, especially for parcellations with subcortical areas included[12,117]. This step only affected the total number of parcels for the Craddock and Aicha parcellations of the human neocortex (i.e., fewer parcels than in the original volume representations).

Brain phenotypes

We used various brain phenotypes specific to the human, macaque, marmoset, and mouse species to compare the regional homogeneity of the geometric and existing benchmark parcellations. All data were obtained from published studies and/or open-access repositories, unless otherwise stated. All data were for the whole brain (includes left and right hemispheres), unless otherwise stated.

Human neocortex

We analyzed resting-state functional MRI (fMRI) FC matrices from three independent datasets [the Human Connectome Project (HCP)[14]; the Genomics Superstructure Project (GSP)[74]; and a dataset acquired in-house at Monash University (Monash)[75]] and 242 non-FC brain maps divided into the following 8 categories: morphometry (1 map); microstructure (3 maps); cytoarchitecture (50 maps); metabolism (5 maps); gene expression (1 map); chemoarchitecture (19 maps); HCP task activation (47 maps); and Neurosynth (116 maps). All data were mapped onto the fsLR_32k surface space, with 32,492 vertices per hemisphere.

The HCP FC matrix was derived from preprocessed resting-state fMRI data acquired in 255 unrelated healthy individuals (ages 22–35; 132 females), which is the largest HCP sample excluding twins or siblings and with all participants having completed resting-state and task-evoked data[14]. In brief, the fMRI parameters were: field strength of 3 T, isotropic voxel size of 2 mm, repetition time (TR) of 720 ms, echo time (TE) of 33.1 ms, left to right encoding direction, and scanning duration of 14.4 min with a total of 1200 time frames. All other acquisition parameters can be found in ref.[14]. Each individual's data were preprocessed by the HCP team via their minimal preprocessing pipeline[118], which included ICA-FIX to correct for structured noise and residual confounds[119], and mapped onto the fsLR_32k surface space. For each participant, we calculated the Pearson correlation coefficient of pairs of vertex-level time series, resulting in a 32,492×32,492 FC matrix per hemisphere. We then took the average of the individual-specific FC matrices across the 255 individuals to construct a group-averaged FC matrix for each hemisphere.

The GSP FC matrix was derived from resting-state fMRI data acquired in 1564 healthy individuals (ages 18–35; 901 females)[74]. In brief, the fMRI parameters were: field strength of 3 T, isotropic voxel size of 3 mm, TR of 3000 ms, TE of 30 ms, and scanning duration of 6.2 min with a total of 124 time frames. All other acquisition parameters can be found in ref.[74]. Each individual's data were preprocessed via the standard pipeline of fMRIPrep v22.0.0[120,121], denoised with ICA-FIX, and mapped onto the fsLR_32k surface space. We then removed the first 5 time frames to stabilize the signal. We then calculated individual-specific FC matrices and took the average across the 1564 individuals to construct a group-averaged 32,492×32,492 FC matrix for each hemisphere.

The Monash FC matrix was derived from multiband resting-state fMRI data acquired in 440 healthy individuals (ages 21; all females)[75]. In brief, the fMRI parameters were: field strength of 3 T, isotropic voxel size of 3 mm, TR of 754 ms, TE of 21 ms, and scanning duration of 7.7 min with a total of 616 time frames. All other acquisition parameters can be found in ref.[75]. Each

individual's data were preprocessed via an in-house pipeline, which included ICA-FIX, global signal regression, and 3 mm spatial smoothing (see ref.[75] for further details of the preprocessing), and mapped onto the fsLR_32k surface space. We then calculated individual-specific FC matrices and took the average across the 440 individuals to construct a group-averaged 32,492×32,492 FC matrix for each hemisphere. The diversity of preprocessing pipelines used across the HCP, GSP, and Monash datasets ensured that our findings are not specific to any single data processing approach.

The morphometry map represents cortical thickness and was obtained from the HCP repository[15]. The 3 microstructure maps represent the ratio of T1w and T2w MRI signal and diffusion MRI-derived estimates of neurite density index (NDI) and orientation dispersion index (ODI). T1w:T2w ratio indirectly quantifies intracortical myeloarchitecture and was obtained from ref.[82], while NDI and ODI respectively quantify the packing density of axons or dendrites and orientational coherence of neurites and were obtained from ref.[122]. The 50 cytoarchitecture maps represent cell density profiles across 50 equidistant layers between the white and pial cortical layers of the BigBrain atlas[123] and were obtained from ref.[124].

The metabolism, gene expression, and chemoarchitecture maps were obtained from the neuromaps repository[80]. The 5 metabolism maps represent positron emission tomography (PET)-based markers of cerebral metabolic rate of glucose (CMRGlu), cerebral blood volume (CBV), cerebral blood flow (CBF), cerebral metabolic rate of oxygen ($CMRO_2$), and synaptic density based on BPnd tracer binding to SV2a[125,126]. The gene expression map represents the first principal component of all genes in the Allen Human Brain atlas[127]. The 19 chemoarchitecture maps represent PET-based densities of neurotransmitter receptors of acetylcholine ($\alpha_4\beta_2$, M_1, and VACht), cannabinoid (CB_1), dopamine (D_1, D_2, and DAT), GABA (GABA-A α_5 subunit), glutamate ($mGluR_5$ and NMDA), histamine (H_3), mu-opioid (MOR), norepinephrine (NET), and serotonin ($5\text{-}HT_{1A}$, $5\text{-}HT_{1B}$, $5\text{-}HT_{2A}$, $5\text{-}HT_4$, $5\text{-}HT_6$, and 5-HTT)[128–146].

The 47 HCP task-activation maps represent unthresholded maps of task activations across 7 task domains of social, motor, gambling, working memory, language, emotion, and relational[147]. Each map represents a key contrast commonly used in the literature that shows the major activation pattern elicited by the task. See refs[58,147] and Supplementary Table 3 for details of each task and contrast. We used the task maps as provided by HCP.

The 116 Neurosynth maps represent the association between voxels and cognitive terms obtained from Neurosynth, a meta-analytical tool that synthesizes results from more than 14,000 published fMRI studies by searching for keywords (e.g., action) published alongside fMRI voxel coordinates[81]. The unthresholded association maps were downloaded from https://neurosynth.org/. Although there are >1000 terms reported in Neurosynth, we only focused on 116 terms that are related to 11 cognition- and behavior-related concepts selected from the Cognitive Atlas[148], which is a public ontology of concepts and terms used in cognitive science. See Supplementary Table 4 for the full list of terms we used.

Macaque neocortex

We analyzed 1 resting-state fMRI FC matrix and 19 non-FC brain maps divided into the following 3 categories: morphometry (1 map); microstructure (1 map); and chemoarchitecture (17 maps). All data were mapped onto the fsLR_10k surface space, with 10,242 vertices per hemisphere.

The FC matrix was derived from preprocessed resting-state fMRI data acquired in 6 individuals[149]. In brief, the fMRI parameters were: field strength of 3 T, isotropic voxel size of 1.25 mm, TR of

2000 ms, TE of 30 ms, and scanning duration of 40 min with a total of 1200 time frames. All other acquisition parameters can be found in ref.[149]. Each individual's data were preprocessed via an HCP-style pipeline adapted to non-human primates (NHP) pipeline (https://github.com/Washington-University/NHPPipelines) and mapped onto the fsLR_10k surface space. We then calculated individual-specific FC matrices and took the average across the 6 individuals to construct a group-averaged 10,242×10,242 FC matrix for each hemisphere.

The morphometry and microstructure maps represent cortical thickness and T1w:T2w ratio, respectively, and were obtained from ref.[150]. The 17 chemoarchitecture maps represent autoradiographic densities in the left hemisphere of neurotransmitter receptors of acetylcholine M_1, M_2, and M_3), dopamine (D_1), GABA (GABA-A, GABA-A/BZ, and GABA-B), glutamate (AMPA, Kainate, and NMDA), noradrenaline (α_1 and α_2), and serotonin (5-HT_{1A}, 5-HT_2) and averaged densities of excitatory (i.e., glutamate), inhibitory (i.e., GABA), and modulatory (i.e., serotonin, acetylcholine, and noradrenaline) receptors. The receptor maps were obtained from ongoing unpublished work, with all receptor density estimates reconstructed via the pipeline described in ref.[151]. Note that the chemoarchitecture maps were only available for the left hemisphere; hence, we restricted the calculation of homogeneity with respect to those maps to the left hemisphere.

Marmoset neocortex

We analyzed resting-state fMRI FC matrices from two independent sites [the Institute of Neuroscience (ION) in China and the National Institutes of Health (NIH) in the USA][152] and 3 non-FC brain maps divided into the following 3 categories: morphometry (1 map); microstructure (1 map); and cytoarchitecture (1 map). All data were mapped onto the fsaverage_38k surface space, with 37,974 and 38,094 vertices for the left and right hemispheres, respectively.

The FC matrices were derived from preprocessed resting-state fMRI data acquired in 10 individuals in each site (i.e., ION and NIH)[152]. In brief, the fMRI parameters for the ION site were: field strength of 9.4 T, isotropic voxel size of 0.5 mm, TR of 2000 ms, TE of 18 ms, right to left encoding direction, and scanning duration of 17.1 min with a total of 512 time frames. The fMRI parameters for the NIH site were: field strength of 7 T, isotropic voxel size of 0.5 mm, TR of 2000 ms, TE of 22.2 ms, right to left encoding direction, and scanning duration of 17.1 min with a total of 512 time frames. All other acquisition parameters can be found in ref.[152]. Each individual's data were preprocessed via the Marmoset Brain Mapping Project's pipeline (see https://marmosetbrainmapping.org/) and mapped onto the fsaverage_38k surface space. For each of the two sites, we then calculated individual-specific FC matrices and took the average across the 10 individuals to construct a group-averaged 37,974×37,974 and 38,094×38,094 FC matrix for the left and right hemispheres, respectively.

The morphometry and microstructure maps represent cortical thickness and T1w:T2w ratio, respectively, and were obtained from ref.[103]. The cytoarchitecture map represents cell density profiles in the left hemisphere derived from Nissl-stains and was obtained from ref.[153]. Note that the cytoarchitecture map was only available for the left hemisphere; hence, we restricted the calculation of homogeneity with respect to that map to the left hemisphere.

Mouse neocortex

We analyzed resting-state FC matrices derived from fMRI[154] and Ca^{2+} imaging[155] and 87 non-FC maps divided into the following 3 categories: microstructure (1 map); cytoarchitecture (1 map); and gene expression (85 maps). All data were mapped onto the Allen Mouse Brain CCFv3

volumetric space with 200 μm isotropic voxel resolution (except for the Ca^{2+} data, which were in 2D space; see below or Supplementary Information S4).

The fMRI FC matrix was derived from preprocessed resting-state fMRI data acquired in 193 individuals[154]. The data were pooled from 17 independent datasets across multiple centers. In brief, the fMRI parameters were: field strengths ranging from 4.7 to 11.7 T, isotropic voxel size of 200 μm, TRs ranging from 1000 to 2000 ms, TEs ranging from 10 to 25 ms, and number of time frames ranging from 150 to 1000. All other acquisition parameters can be found in ref.[154]. All data were preprocessed via a unified pipeline (see ref.[154] for further details of the preprocessing) and mapped onto the CCFv3 volumetric space. We then calculated individual-specific FC matrices and took the average across the 193 individuals to construct a group-averaged voxel-level FC matrix for each hemisphere.

The Ca^{2+} FC matrix was derived from preprocessed resting-state cortex-wide fluorescence Ca^{2+} data acquired in 9 individuals[155]. In brief, the Ca^{2+} data were recorded using an in-house fiberscope[155] and an sCMOS camera (512×512 pixels). The acquisition interleaved cyan (470/24, Ca^{2+}-sensitive) and violet (395/25, Ca^{2+}-insensitive) wavelengths using a Lumencor (LLE 7Ch Controller) light source at 20 Hz. The violet wavelength was for measuring background noise, which was regressed from the cyan data to obtain the final data at 10 Hz temporal resolution. The resulting images have a 25×25 μm resolution. The exposure time of each wavelength (violet and cyan) was 40 ms to avoid artifacts caused by the rolling shutter. All other acquisition parameters and preprocessing can be found in ref.[155]. Since the Ca^{2+} data were in 2D space, we projected the Allen Mouse Brain Atlas (i.e., ABA80 in Fig. 3A) and the corresponding geometric parcellation in 3D volume space to the 2D imaging plane of the Ca^{2+} data. See Supplementary Information S4 for further details about the imaging data, preprocessing, and volume-to-2D plane projection of the parcellations. We then calculated individual-specific FC matrices for each hemisphere. We used the pixel-level FC matrices and 2D plane-projected parcellations to calculate regional homogeneity for each individual, which we then averaged for the final analysis.

The microstructure map represents T1w:T2w ratio and was obtained from refs[156,157]. The cytoarchitecture map represents cell density profiles derived from Nissl-stains and was obtained from ref.[158]. The 85 gene expression maps represent gene-expression profiles and were obtained from ref.[159]. Although there are >4000 gene-expression maps available from the above dataset, we restricted our analysis to 85 brain-related genes expressed in the brain chosen based on the criteria developed in ref.[157]. See Supplementary Table 5 for the list of genes we analyzed.

Human non-neocortical structures

We analyzed the same three independent resting-state fMRI datasets used for the human neocortex (i.e., HCP, GSP, and Monash). We analyzed the data in their original volumetric space smoothed with a full width at half maximum (FWHM) of 6 mm and then constructed a group-averaged voxel-level FC matrix for each hemisphere of each non-neocortical structure.

Null FC matrices

In Fig. 1E, we used the eigenstrapping method to randomize fMRI data and generate null FC matrices[78] (see Supplementary Information S2.1 for details). We first generated 1000 randomly rotated surrogate geometric eigenmodes of the human neocortical surface, separately for the left and right hemispheres (Supplementary Fig. 3A). We applied the surrogate eigenmodes to reconstruct each time volume of each individual's fMRI (Supplementary Fig. 3B), effectively

creating 1000 surrogates of the vertex by time fMRI data. Note that the same set of rotated eigenmodes was used across individuals. For each surrogate, we calculated individual-specific FC matrices and took the average across the individuals to construct 1000 null group-averaged FC matrices for each hemisphere. This approach generates a randomized map that retains the exact spatial and temporal autocorrelation of the original data without relying on heuristics employed in other popular methods, such as the Spin test[79,160,161], that could affect proper statistical inference on brain data[78,162,163]. We nonetheless replicate our null findings using the Spin test for completeness (see Supplementary Information S2.2 and Supplementary Figure 4).

Reaction-diffusion model

Reaction-diffusion models are used ubiquitously to study various forms of biological pattern formation[164]. The generalized model of two coupled molecules, u and v, spatiotemporally diffusing and reacting in a system is commonly defined in terms of the following equations[60,61]:

$$\frac{\partial u(\mathbf{r},t)}{\partial t} = f(u(\mathbf{r},t), v(\mathbf{r},t)) + D_u \nabla^2 u(\mathbf{r},t)\,, \tag{5}$$

$$\frac{\partial v(\mathbf{r},t)}{\partial t} = g(u(\mathbf{r},t), v(\mathbf{r},t)) + D_v \nabla^2 v(\mathbf{r},t)\,, \tag{6}$$

where $u(\mathbf{r},t)$ and $v(\mathbf{r},t)$ denote the local concentration of molecules u and v, respectively, at spatial location $\mathbf{r}$ at time t. For brevity, we will drop the $(\mathbf{r},t)$ in subsequent equations, but u and v are treated as functions in space and time, unless otherwise stated. The terms $f(u,v)$ and $g(u,v)$ model the reactions of the molecules (e.g., production and elimination of concentrations), while the terms $D_u\nabla^2 u$ and $D_v\nabla^2 v$ model the diffusion of the molecules with D_u and D_v being positive diffusion constants. Assuming the molecules have uniform concentrations at equilibrium, solutions that depart from the equilibrium can be obtained as follows (see Supplementary Information S1.1 for the derivation):

$$\frac{\partial u}{\partial t} = au - bv + D_u \nabla^2 u, \tag{7}$$

$$\frac{\partial v}{\partial t} = cu - dv + D_v \nabla^2 v. \tag{8}$$

By setting the constants a, b, c, and d as positive numbers, the form of Eqs (7) and (8) assigns molecule u as the activator and molecule v as the inhibitor. Turing has shown that certain regimes of the model's parameters (e.g., inhibitor diffuses much faster than the activator) can destabilize the uniform stationary states of the molecules' concentrations, leading to the spontaneous emergence of a spatially non-constant solution at equilibrium that defines a spatial pattern, called a Turing instability[41], that can mimic various patterns found in nature (e.g., leopard spots, zebra stripes; see refs[61,165] for a collection of related articles). One can show that it is the relation between the model constants, and not their specific values, that give rise to spatial Turing instabilities (see Supplementary Information S1.2 for the derivation). Specifically, instabilities will occur as long as the model constants satisfy all of the following conditions: $D_u < D_v$; $a < d$; $ad < bc$; and $\frac{d}{D_v} < \frac{a}{D_u}$.

In Fig. 6, we simulated the model in Eqs (7) and (8) on the left hemisphere of the human neocortex, seeding molecules u and v at distinct areas defined by the HCP-MMP1 atlas (i.e., Glasser360 in Fig. 1C)[2]. The example steady-state solution in Fig. 6B (top row) with Turing instability was obtained using the parameters: $a = 2$; $b = 4$; $c = 2$; $d = 3$; $D_u = 50$; and $D_v = 100$.

We reiterate that the spatial pattern of the instability shown in Fig. 6B is invariant to the specific values of these parameters as long as the model parameter combinations meet the conditions defined above for the instability to emerge. Moreover, our hierarchical algorithm need not necessarily result from a reaction-diffusion process, given prior work demonstrating that a bipartition could be obtained using a single diffusion gradient (as in Wolpert's French Flag Problem[99,10]). This invariance to model parameters and dynamics supports the robustness of the underlying process of recursive bipartition based on geometry and suggests that multiple mechanisms may achieve the same end. We used an activator-inhibitor reaction-diffusion process here given evidence that some areal patterning molecules are mutually antagonistic (e.g., see refs[85,166,167]), but acknowledge that this is not the only process that may achieve the end results we describe. Indeed, experimental studies have shown that morphogen gradients can delineate regional tissue boundaries using a variety of physiological processes[52] and that the actual processes driving the regional patterning of the brain are likely complex, involving time-dependent interactions between multiple molecular signals[48,51,168]. We used a basic reaction-diffusion model here to demonstrate a simple mechanism through which geometric constraints via eigenmodes[58,59] can plausibly give rise to the multiscale regional architecture implied by our parcellation algorithm, and we welcome further work that improves on the physiological plausibility of this mechanism.

Data availability

All source data to generate the results of the study and species-specific geometric parcellations of varying resolutions will be made openly available at https://github.com/NSBLab/geometric_parcellation upon publication.

Code availability

All computer codes to generate the parcellations, analyze results, and reproduce the figures of the study will be made openly available at https://github.com/NSBLab/geometric_parcellation upon publication.

Acknowledgements

This work was supported by the MASSIVE HPC facility (www.massive.og.au). J.C.P. was supported by the National Health and Medical Research Council (2034000), Monash FMNHS Early Career Postdoctoral Fellowship, and Monash FMNHS Early Career Research Excellence Program. M.M. was supported by the SNSF Postdoc Mobility Grant (214392). N.P.-G. was supported by the Helmholtz Association's Initiative and Networking Fund through the Helmholtz International BigBrain Analytics and Learning Laboratory (HIBALL) under the Helmholtz International Lab grant agreement InterLabs-0015. B.T.T.Y. was supported by the NUS Yong Loo Lin School of Medicine (NUHSRO/2020/124/TMR/LOA), Singapore National Medical Research Council (NMRC) LCG (OFLCG19May-0035), NMRC CTG-IIT (CTGIIT23jan-0001), NMRC

OF-IRG (OFIRG24jan-0030), NMRC STaR (STaR20nov-0003), Singapore Ministry of Health (MOH) Centre Grant (CG21APR1009), the Temasek Foundation (TF2223-IMH-01), and United States National Institutes of Health (R01MH133334). M.A.B. was supported by the National Health and Medical Research Council (1154378, 1146292, 1045354, 1006573). M.B. was supported by the National Health and Medical Research Council (2008612). A.F. was supported by the Australian Research Council (FL220100184), National Health and Medical Research Council (1197431), and Sylvia and Charles Viertel Charitable Foundation (2017042).

Author contributions

J.C.P., P.A.R., K.M.A., and A.F. conceptualized the study. J.C.P., P.A.R., and A.F. designed the methodology. J.C.P., P.A.R., and A.F. performed the investigation. M.M. and X.S. analyzed the mouse calcium imaging data. P.T.L., A.H., T.F., N.P.-G., J.T., M.A.B., R.T.C., and E.L. contributed with data and data processing. P.A.R., R.K., B.T.T.Y., and M.B. provided intellectual input to data analysis. J.C.P. and A.F. administered the project. J.C.P. developed the visualizations. A.F. acquired funding. A.F. supervised the project. J.C.P. and A.F. wrote the original draft. All authors reviewed and edited the final manuscript.

Competing interests

K.M.A. is the scientific advisor and a shareholder in BrainKey Inc., a medical image analysis software company. The other authors declare no competing interests.

References

1. Brodmann, K. Vergleichende Lokalisationslehre der Grosshirnrinde in ihren Prinzipien dargestellt auf Grund des Zellenbaues von Dr. K. Brodmann ... (J.A. Barth, 1909).
2. Glasser, M. F. et al. A multi-modal parcellation of human cerebral cortex. Nature **536**, 171–178 (2016).
3. Petersen, S. E., Seitzman, B. A., Nelson, S. M., Wig, G. S. & Gordon, E. M. Principles of cortical areas and their implications for neuroimaging. Neuron **112**, 2837–2853 (2024).
4. Bullmore, E. & Sporns, O. Complex brain networks: Graph theoretical analysis of structural and functional systems. Nature Reviews Neuroscience **10**, 186–198 (2009).
5. Fornito, A., Zalesky, A. & Bullmore, E. T. Fundamentals of Brain Network Analysis. (2016).
6. Zilles, K. & Amunts, K. Centenary of Brodmann's map — conception and fate. Nat Rev Neurosci **11**, 139–145 (2010).
7. Bailey, P. & von Bonin, G. The Isocortex of Man. (University of Illinois Press, 1951).
8. Kaas, J. H. The Organization of Neocortex in Mammals: Implications for Theories of Brain Function. Annual Review of Psychology **38**, 129–151 (1987).
9. Lashley, K. S. & Clark, G. The cytoarchitecture of the cerebral cortex of ateles: A critical examination of architectonic studies. Journal of Comparative Neurology **85**, 223–305 (1946).
10. Eickhoff, S. B., Yeo, B. T. T. & Genon, S. Imaging-based parcellations of the human brain. Nature Reviews Neuroscience **19**, 672–686 (2018).
11. Fan, L. et al. The Human Brainnetome Atlas: A New Brain Atlas Based on Connectional Architecture. Cerebral Cortex **26**, 3508–3526 (2016).

12. Schaefer, A. et al. Local-global parcellation of the human cerebral cortex from intrinsic functional connectivity mri. Cerebral Cortex **28**, 3095–3114 (2018).
13. Van Essen, D. C. et al. Cerebral cortical folding, parcellation, and connectivity in humans, nonhuman primates, and mice. Proceedings of the National Academy of Sciences **116**, 26173–26180 (2019).
14. van Essen, D. C. et al. The WU-Minn Human Connectome Project: An overview. NeuroImage **80**, 62–79 (2013).
15. Huntenburg, J. M., Bazin, P.-L. & Margulies, D. S. Large-Scale Gradients in Human Cortical Organization. Trends in Cognitive Sciences **22**, 21–31 (2018).
16. Margulies, D. S. et al. Situating the default-mode network along a principal gradient of macroscale cortical organization. Proceedings of the National Academy of Sciences of the United States of America **113**, 12574–12579 (2016).
17. Wang, X.-J. Macroscopic gradients of synaptic excitation and inhibition in the neocortex. Nat Rev Neurosci **21**, 169–178 (2020).
18. Amunts, K. & Zilles, K. Architectonic Mapping of the Human Brain beyond Brodmann. Neuron **88**, 1086–1107 (2015).
19. Benisty, H. et al. Rapid fluctuations in functional connectivity of cortical networks encode spontaneous behavior. Nat Neurosci **27**, 148–158 (2024).
20. Salehi, M. et al. There is no single functional atlas even for a single individual: Functional parcel definitions change with task. NeuroImage **208**, 116366 (2020).
21. Salehi, M., Karbasi, A., Barron, D. S., Scheinost, D. & Constable, R. T. Individualized functional networks reconfigure with cognitive state. NeuroImage **206**, 116233 (2020).
22. Betzel, R. F. & Bassett, D. S. Multi-scale brain networks. NeuroImage **160**, 73–83 (2017).
23. Luo, W. & Constable, R. T. Inside information: Systematic within-node functional connectivity changes observed across tasks or groups. NeuroImage **247**, 118792 (2022).
24. Pines, A. R. et al. Dissociable multi-scale patterns of development in personalized brain networks. Nat Commun **13**, 2647 (2022).
25. Abbie, A. A. Cortical lamination in a polyprotodont marsupial, Perameles nasuta. Journal of Comparative Neurology **76**, 509–536 (1942).
26. Barbas, H. Pattern in the laminar origin of corticocortical connections. Journal of Comparative Neurology **252**, 415–422 (1986).
27. Dart, R. A. The Dual Structure of the Neopallium: its History and Significance. J Anat **69**, 3–19 (1934).
28. García-Cabezas, M. Á., Zikopoulos, B. & Barbas, H. The Structural Model: a theory linking connections, plasticity, pathology, development and evolution of the cerebral cortex. Brain Struct Funct **224**, 985–1008 (2019).
29. García-Cabezas, M. Á., Hacker, J. L. & Zikopoulos, B. A Protocol for Cortical Type Analysis of the Human Neocortex Applied on Histological Samples, the Atlas of Von Economo and Koskinas, and Magnetic Resonance Imaging. Front. Neuroanat. **14**, (2020).
30. Smith, S. M. et al. Temporally-independent functional modes of spontaneous brain activity. Proceedings of the National Academy of Sciences **109**, 3131–3136 (2012).
31. Vincent, J. L. et al. Intrinsic functional architecture in the anaesthetized monkey brain. Nature **447**, 83–86 (2007).
32. Yeo, B. T. T. et al. The organization of the human cerebral cortex estimated by intrinsic functional connectivity. Journal of Neurophysiology **106**, 1125–1165 (2011).
33. Mountcastle, V. B. The columnar organization of the neocortex. Brain **120**, 701–722 (1997).

1090 34. Haak, K. V. & Beckmann, C. F. Understanding brain organisation in the face of functional
1091 heterogeneity and functional multiplicity. NeuroImage **220**, 117061 (2020).
1092 35. Halassa, M. M. & Sherman, S. M. Thalamocortical Circuit Motifs: A General Framework.
1093 Neuron **103**, 762–770 (2019).
1094 36. Toro, R. & Burnod, Y. Geometric atlas: modeling the cortex as an organized surface.
1095 NeuroImage **20**, 1468–1484 (2003).
1096 37. Auzias, G., Coulon, O. & Brovelli, A. MarsAtlas: A cortical parcellation atlas for functional
1097 mapping. Human Brain Mapping **37**, 1573–1592 (2016).
1098 38. Qiu, A., Younes, L. & Miller, M. I. Intrinsic and extrinsic analysis in computational
1099 anatomy. NeuroImage **39**, 1803–1814 (2008).
1100 39. Katagiri, T. & Watabe, T. Bone Morphogenetic Proteins. Cold Spring Harb Perspect Biol **8**,
1101 a021899 (2016).
1102 40. Toyoda, R. et al. FGF8 acts as a classic diffusible morphogen to pattern the neocortex.
1103 Development **137**, 3439–3448 (2010).
1104 41. Turing, A. M. The chemical basis of morphogenesis. Philosophical Transactions of the Royal
1105 Society of London. Series B, Biological Sciences **237**, 37–72 (1952).
1106 42. Kiecker, C. & Lumsden, A. Compartments and their boundaries in vertebrate brain
1107 development. Nat Rev Neurosci **6**, 553–564 (2005).
1108 43. Briscoe, J. & Small, S. Morphogen rules: design principles of gradient-mediated embryo
1109 patterning. Development **142**, 3996–4009 (2015).
1110 44. Garel, S., Huffman, K. J. & Rubenstein, J. L. R. Molecular regionalization of the neocortex
1111 is disrupted in Fgf8hypomorphic mutants. Development **130**, 1903–1914 (2003).
1112 45. Greig, L. C., Woodworth, M. B., Galazo, M. J., Padmanabhan, H. & Macklis, J. D.
1113 Molecular logic of neocortical projection neuron specification, development and diversity.
1114 Nat Rev Neurosci **14**, 755–769 (2013).
1115 46. Grove, E. A. & Fukuchi-Shimogori, T. Generating the Cerebral Cortical Area Map. Annual
1116 Review of Neuroscience **26**, 355–380 (2003).
1117 47. Grove, E. A. & Monuki, E. S. Chapter 1 - Morphogens, patterning centers, and their
1118 mechanisms of action. in Patterning and Cell Type Specification in the Developing CNS
1119 and PNS (Second Edition) (eds. Rubenstein, J., Rakic, P., Chen, B. & Kwan, K. Y.) 3–21
1120 (Academic Press, 2020). doi:10.1016/B978-0-12-814405-3.00001-1.
1121 48. O'Leary, D. D. M., Chou, S.-J. & Sahara, S. Area Patterning of the Mammalian Cortex.
1122 Neuron **56**, 252–269 (2007).
1123 49. O'Leary, D. D. M. & Nakagawa, Y. Patterning centers, regulatory genes and extrinsic
1124 mechanisms controlling arealization of the neocortex. Current Opinion in Neurobiology **12**,
1125 14–25 (2002).
1126 50. Alfano, C. & Studer, M. Neocortical arealization: Evolution, mechanisms, and open
1127 questions. Developmental Neurobiology **73**, 411–447 (2013).
1128 51. Cadwell, C. R., Bhaduri, A., Mostajo-Radji, M. A., Keefe, M. G. & Nowakowski, T. J.
1129 Development and Arealization of the Cerebral Cortex. Neuron **103**, 980–1004 (2019).
1130 52. Lander, A. D. Morpheus Unbound: Reimagining the Morphogen Gradient. Cell **128**, 245–
1131 256 (2007).
1132 53. Rakic, P. Specification of cerebral cortical areas. Science **241**, 170–176 (1988).
1133 54. Wolpert, L. One hundred years of positional information. Trends in Genetics **12**, 359–364
1134 (1996).
1135 55. Hébert, J. M., Mishina, Y. & McConnell, S. K. BMP Signaling Is Required Locally to
1136 Pattern the Dorsal Telencephalic Midline. Neuron **35**, 1029–1041 (2002).

56. Kimelman, D. & Martin, B. L. Anterior–posterior patterning in early development: three strategies. WIREs Developmental Biology **1**, 253–266 (2012).
57. Rubenstein, J. L. R. et al. Genetic Control of Cortical Regionalization and Connectivity. Cerebral Cortex **9**, 524–532 (1999).
58. Pang, J. C. et al. Geometric constraints on human brain function. Nature **618**, 566–574 (2023).
59. Robinson, P. A. et al. Eigenmodes of brain activity: Neural field theory predictions and comparison with experiment. NeuroImage **142**, 79–98 (2016).
60. Murray, J. D. Mathematical Biology II: Spatial Models and Biomedical Applications. (Springer, Berlin Heidelberg u.a, 2003).
61. Hoyle, R. Pattern Formation: An Introduction to Methods. (Cambridge University Press, Cambridge, 2006). doi:10.1017/CBO9780511616051.
62. Delgado, I. & Torres, M. Gradients, waves and timers, an overview of limb patterning models. Seminars in Cell & Developmental Biology **49**, 109–115 (2016).
63. Iber, D. & Menshykau, D. The control of branching morphogenesis. Open Biology **3**, 130088 (2013).
64. Newman, S. A. & Bhat, R. Activator-inhibitor dynamics of vertebrate limb pattern formation. Birth Defects Research Part C: Embryo Today: Reviews **81**, 305–319 (2007).
65. Saunders, P. T. & Ho, M. W. Reliable segmentation by successive bifurcation. Bltn Mathcal Biology **57**, 539–556 (1995).
66. West, G. B., Brown, J. H. & Enquist, B. J. A General Model for the Origin of Allometric Scaling Laws in Biology. Science **276**, 122–126 (1997).
67. Striedter. Principles Of Brain Evolution. (Oxford University Press USA, Sunderland, Mass, 2004).
68. Puelles, L. & Medina, L. Field homology as a way to reconcile genetic and developmental variability with adult homology. Brain Research Bulletin **57**, 243–255 (2002).
69. Nelson, C. M., VanDuijn, M. M., Inman, J. L., Fletcher, D. A. & Bissell, M. J. Tissue Geometry Determines Sites of Mammary Branching Morphogenesis in Organotypic Cultures. Science **314**, 298–300 (2006).
70. Craddock, R. C., James, G. A., Holtzheimer III, P. E., Hu, X. P. & Mayberg, H. S. A whole brain fMRI atlas generated via spatially constrained spectral clustering. Human Brain Mapping **33**, 1914–1928 (2012).
71. Shen, X., Tokoglu, F., Papademetris, X. & Constable, R. T. Groupwise whole-brain parcellation from resting-state fMRI data for network node identification. NeuroImage **82**, 403–415 (2013).
72. Gordon, E. M. et al. Generation and Evaluation of a Cortical Area Parcellation from Resting-State Correlations. Cerebral Cortex **26**, 288–303 (2016).
73. Tian, Y., Margulies, D. S., Breakspear, M. & Zalesky, A. Topographic organization of the human subcortex unveiled with functional connectivity gradients. Nature Neuroscience **23**, 1421–1432 (2020).
74. Holmes, A. J. et al. Brain Genomics Superstruct Project initial data release with structural, functional, and behavioral measures. Sci Data **2**, 150031 (2015).
75. Sabaroedin, K. et al. Functional Connectivity of Corticostriatal Circuitry and Psychosis-like Experiences in the General Community. Biological Psychiatry **86**, 16–24 (2019).
76. Schaefer, A. et al. Local-Global Parcellation of the Human Cerebral Cortex from Intrinsic Functional Connectivity MRI. Cerebral Cortex **28**, 3095–3114 (2018).

77. Wedeen, V. J. et al. The Geometric Structure of the Brain Fiber Pathways. Science **335**, 1628–1634 (2012).
78. Koussis, N. C. et al. Generation of surrogate brain maps preserving spatial autocorrelation through random rotation of geometric eigenmodes. 2024.02.07.579070 Preprint at https://doi.org/10.1101/2024.02.07.579070 (2024).
79. Alexander-Bloch, A. F. et al. On testing for spatial correspondence between maps of human brain structure and function. NeuroImage **178**, 540–551 (2018).
80. Markello, R. D. et al. neuromaps: structural and functional interpretation of brain maps. Nat Methods **19**, 1472–1479 (2022).
81. Yarkoni, T., Poldrack, R. A., Nichols, T. E., Van Essen, D. C. & Wager, T. D. Large-scale automated synthesis of human functional neuroimaging data. Nat Methods **8**, 665–670 (2011).
82. Glasser, M. F. & Van Essen, D. C. Mapping Human Cortical Areas In Vivo Based on Myelin Content as Revealed by T1- and T2-Weighted MRI. Journal of Neuroscience **31**, 11597–11616 (2011).
83. Arslan, S. et al. Human brain mapping: A systematic comparison of parcellation methods for the human cerebral cortex. NeuroImage **170**, 5–30 (2018).
84. Schwartz, E. et al. Evolution of cortical geometry and its link to function, behaviour and ecology. Nat Commun **14**, 2252 (2023).
85. Feng, J. et al. COUP-TFI specifies the medial entorhinal cortex identity and induces differential cell adhesion to determine the integrity of its boundary with neocortex. Science Advances **7**, eabf6808 (2021).
86. Quiñinao, C., Prochiantz, A. & Touboul, J. Local homeoprotein diffusion can stabilize boundaries generated by graded positional cues. Development **142**, 1860–1868 (2015).
87. Rosa, M. G. P. & Tweedale, R. Brain maps, great and small: lessons from comparative studies of primate visual cortical organization. Philosophical Transactions of the Royal Society B: Biological Sciences (2005) doi:10.1098/rstb.2005.1626.
88. Lein, E. S., Belgard, T. G., Hawrylycz, M. & Molnár, Z. Transcriptomic Perspectives on Neocortical Structure, Development, Evolution, and Disease. Annual Review of Neuroscience **40**, 629–652 (2017).
89. Rakic, P. Neurogenesis in adult primate neocortex: an evaluation of the evidence. Nat Rev Neurosci **3**, 65–71 (2002).
90. Mosby, L. S., Bowen, A. E. & Hadjivasiliou, Z. Morphogens in the evolution of size, shape and patterning. Development **151**, dev202412 (2024).
91. Gordon, N. K., Chen, Z., Gordon, R. & Zou, Y. French flag gradients and Turing reaction-diffusion versus differentiation waves as models of morphogenesis. Biosystems **196**, 104169 (2020).
92. Wolpert, L. Positional information and the spatial pattern of cellular differentiation. Journal of Theoretical Biology **25**, 1–47 (1969).
93. Struhl, G., Struhl, K. & Macdonald, P. M. The gradient morphogen bicoid is a concentration-dependent transcriptional activator. Cell **57**, 1259–1273 (1989).
94. Struhl, G., Johnston, P. & Lawrence, P. A. Control of Drosophila body pattern by the hunchback morphogen gradient. Cell **69**, 237–249 (1992).
95. Striedter, G. F. Epigenesis and Evolution of Brains: From Embryonic Divisions to Functional Systems. (2003) doi:10.7551/mitpress/5182.003.0023.

96. Cahalane, D. J., Charvet, C. J. & Finlay, B. L. Modeling local and cross-species neuron number variations in the cerebral cortex as arising from a common mechanism. Proceedings of the National Academy of Sciences **111**, 17642–17647 (2014).
97. Charvet, C. J., Cahalane, D. J. & Finlay, B. L. Systematic, cross-cortex variation in neuron numbers in rodents and primates. Cerebral Cortex **25**, 147–160 (2015).
98. Lefèvre, J. & Mangin, J.-F. A Reaction-Diffusion Model of Human Brain Development. PLOS Computational Biology **6**, e1000749 (2010).
99. Zagorski, M. et al. Decoding of position in the developing neural tube from antiparallel morphogen gradients. Science **356**, 1379–1383 (2017).
100. Vetter, R. & Iber, D. Precision of morphogen gradients in neural tube development. Nat Commun **13**, 1145 (2022).
101. Fischl, B., Sereno, M. I., Tootell, R. B. H. & Dale, A. M. High-resolution intersubject averaging and a coordinate system for the cortical surface. Human Brain Mapping **8**, 272–284 (1999).
102. Donahue, C. J. et al. Using Diffusion Tractography to Predict Cortical Connection Strength and Distance: A Quantitative Comparison with Tracers in the Monkey. J. Neurosci. **36**, 6758–6770 (2016).
103. Liu, C. et al. Marmoset Brain Mapping V3: Population multi-modal standard volumetric and surface-based templates. NeuroImage **226**, 117620 (2021).
104. Wachinger, C., Golland, P., Kremen, W., Fischl, B. & Reuter, M. BrainPrint: A discriminative characterization of brain morphology. NeuroImage **109**, 232–248 (2015).
105. Chavel, I. Eigenvalues in Riemannian Geometry. (Academic Press, 1984).
106. Reuter, M., Wolter, F. E. & Peinecke, N. Laplace-Beltrami spectra as 'Shape-DNA' of surfaces and solids. CAD Computer Aided Design **38**, 342–366 (2006).
107. Goscinski, W. J. et al. The multi-modal Australian ScienceS Imaging and Visualization Environment (MASSIVE) high performance computing infrastructure: applications in neuroscience and neuroinformatics research. Frontiers in Neuroinformatics **8**, (2014).
108. Gabay, N. C. & Robinson, P. A. Cortical geometry as a determinant of brain activity eigenmodes: Neural field analysis. Physical Review E **96**, (2017).
109. Crampin, E. J., Hackborn, W. W. & Maini, P. K. Pattern formation in reaction-diffusion models with nonuniform domain growth. Bull. Math. Biol. **64**, 747–769 (2002).
110. Crampin, E. J., Gaffney, E. A. & Maini, P. K. Reaction and diffusion on growing domains: Scenarios for robust pattern formation. Bull. Math. Biol. **61**, 1093–1120 (1999).
111. Li, D. et al. Topographic Axes of Wiring Space Converge to Genetic Topography in Shaping Human Cortical Layout. 2023.09.06.556618 Preprint at https://doi.org/10.1101/2023.09.06.556618 (2024).
112. Christian, J. L. Morphogen gradients in development: from form to function. WIREs Developmental Biology **1**, 3–15 (2012).
113. Zhi, D., King, M., Hernandez-Castillo, C. R. & Diedrichsen, J. Evaluating brain parcellations using the distance-controlled boundary coefficient. Human Brain Mapping **43**, 3706 (2022).
114. Jeganathan, J. et al. Spurious correlations in surface-based functional brain imaging. 2024.07.09.602799 Preprint at https://doi.org/10.1101/2024.07.09.602799 (2024).
115. Pijnenburg, R. et al. Myelo- and cytoarchitectonic microstructural and functional human cortical atlases reconstructed in common MRI space. NeuroImage **239**, 118274 (2021).

116. Van Essen, D. C., Glasser, M. F., Dierker, D. L. & Harwell, J. Cortical Parcellations of the Macaque Monkey Analyzed on Surface-Based Atlases. Cereb Cortex **22**, 2227–2240 (2012).
117. Yan, X. et al. Homotopic local-global parcellation of the human cerebral cortex from resting-state functional connectivity. NeuroImage **273**, 120010 (2023).
118. Smith, S. et al. The minimal preprocessing pipelines for the Human Connectome Project. NeuroImage **80**, 105–124 (2013).
119. Salimi-Khorshidi, G. et al. Automatic denoising of functional MRI data: combining independent component analysis and hierarchical fusion of classifiers. Neuroimage **15**, 449–468 (2013).
120. Esteban, O. et al. fMRIPrep: a robust preprocessing pipeline for functional MRI. Nat Methods **16**, 111–116 (2019).
121. Pavlovich, K., Pang, J., Holmes, A., Constable, T. & Fornito, A. The efficacy of resting-state fMRI denoising pipelines for motion correction and behavioural prediction. 2024.12.01.626250 Preprint at https://doi.org/10.1101/2024.12.01.626250 (2024).
122. Fukutomi, H. et al. Neurite imaging reveals microstructural variations in human cerebral cortical gray matter. Neuroimage **182**, 488–499 (2018).
123. Amunts, K. et al. BigBrain: An Ultrahigh-Resolution 3D Human Brain Model. Science **340**, 1472–1475 (2013).
124. Paquola, C. et al. The BigBrainWarp toolbox for integration of BigBrain 3D histology with multimodal neuroimaging. eLife **10**, e70119 (2021).
125. Finnema, S. J. et al. Kinetic evaluation and test–retest reproducibility of [11C]UCB-J, a novel radioligand for positron emission tomography imaging of synaptic vesicle glycoprotein 2A in humans. J Cereb Blood Flow Metab **38**, 2041–2052 (2018).
126. Vaishnavi, S. N. et al. Regional aerobic glycolysis in the human brain. Proc Natl Acad Sci U S A **107**, 17757–17762 (2010).
127. Hawrylycz, M. J. et al. An anatomically comprehensive atlas of the adult human brain transcriptome. Nature **489**, 391–399 (2012).
128. Aghourian, M. et al. Quantification of brain cholinergic denervation in Alzheimer's disease using PET imaging with [18F]-FEOBV. Mol Psychiatry **22**, 1531–1538 (2017).
129. Bedard, M.-A. et al. Brain cholinergic alterations in idiopathic REM sleep behaviour disorder: a PET imaging study with 18F-FEOBV. Sleep Medicine **58**, 35–41 (2019).
130. Beliveau, V. et al. A High-Resolution In Vivo Atlas of the Human Brain's Serotonin System. J Neurosci **37**, 120–128 (2017).
131. Ding, Y.-S. et al. PET Imaging of the Effects of Age and Cocaine on the Norepinephrine Transporter in the Human Brain Using (S,S)-[11C]O-Methylreboxetine and HRRT. Synapse **64**, 30–38 (2010).
132. DuBois, J. M. et al. Characterization of age/sex and the regional distribution of mGluR5 availability in the healthy human brain measured by high-resolution [(11)C]ABP688 PET. Eur J Nucl Med Mol Imaging **43**, 152–162 (2016).
133. Dukart, J. et al. Cerebral blood flow predicts differential neurotransmitter activity. Sci Rep **8**, 4074 (2018).
134. Gallezot, J.-D. et al. Kinetic modeling of the serotonin 5-HT1B receptor radioligand [11C]P943 in humans. J Cereb Blood Flow Metab **30**, 196–210 (2010).
135. Hansen, J. Y. et al. Mapping neurotransmitter systems to the structural and functional organization of the human neocortex. Nat Neurosci **25**, 1569–1581 (2022).

136. Hillmer, A. T. et al. Imaging of cerebral α4β2* nicotinic acetylcholine receptors with (−)-[18F]Flubatine PET: Implementation of bolus plus constant infusion and sensitivity to acetylcholine in human brain. Neuroimage **141**, 71–80 (2016).
137. Kaller, S. et al. Test-retest measurements of dopamine D1-type receptors using simultaneous PET/MRI imaging. Eur J Nucl Med Mol Imaging **44**, 1025–1032 (2017).
138. Kantonen, T. et al. Interindividual variability and lateralization of μ-opioid receptors in the human brain. Neuroimage **217**, 116922 (2020).
139. Naganawa, M. et al. First in Human Assessment of the Novel M1 Muscarinic Acetylcholine Receptor PET Radiotracer 11C-LSN3172176. Journal of Nuclear Medicine (2020) doi:10.2967/jnumed.120.246967.
140. Nørgaard, M. et al. A high-resolution in vivo atlas of the human brain's benzodiazepine binding site of GABAA receptors. Neuroimage **232**, 117878 (2021).
141. Normandin, M. D. et al. Imaging the cannabinoid CB1 receptor in humans with [11C]OMAR: assessment of kinetic analysis methods, test–retest reproducibility, and gender differences. J Cereb Blood Flow Metab **35**, 1313–1322 (2015).
142. Radhakrishnan, R. et al. Age-Related Change in 5-HT6 Receptor Availability in Healthy Male Volunteers Measured with 11C-GSK215083 PET. J Nucl Med **59**, 1445–1450 (2018).
143. Sandiego, C. M. et al. Reference region modeling approaches for amphetamine challenge studies with [11C]FLB 457 and PET. J Cereb Blood Flow Metab **35**, 623–629 (2015).
144. Savli, M. et al. Normative database of the serotonergic system in healthy subjects using multi-tracer PET. Neuroimage **63**, 447–459 (2012).
145. Smart, K. et al. Sex differences in [11C]ABP688 binding: a positron emission tomography study of mGlu5 receptors. Eur J Nucl Med Mol Imaging **46**, 1179–1183 (2019).
146. Smith, C. T. et al. Partial-volume correction increases estimated dopamine D2-like receptor binding potential and reduces adult age differences. J Cereb Blood Flow Metab **39**, 822–833 (2019).
147. Barch, D. M. et al. Function in the human connectome: Task-fMRI and individual differences in behavior. NeuroImage **80**, 169–189 (2013).
148. Poldrack, R. A. et al. The Cognitive Atlas: Toward a Knowledge Foundation for Cognitive Neuroscience. Front. Neuroinform. **5**, (2011).
149. Autio, J. A. et al. Towards HCP-Style macaque connectomes: 24-Channel 3T multi-array coil, MRI sequences and preprocessing. NeuroImage **215**, 116800 (2020).
150. Hayashi, T. et al. The nonhuman primate neuroimaging and neuroanatomy project. NeuroImage **229**, 117726 (2021).
151. Funck, T. et al. 3D reconstruction of ultra-high resolution neurotransmitter receptor atlases in human and non-human primate brains. 2022.11.18.517039 Preprint at https://doi.org/10.1101/2022.11.18.517039 (2022).
152. Tian, X. et al. An integrated resource for functional and structural connectivity of the marmoset brain. Nat Commun **13**, 7416 (2022).
153. Majka, P. et al. Histology-Based Average Template of the Marmoset Cortex With Probabilistic Localization of Cytoarchitectural Areas. NeuroImage **226**, 117625 (2021).
154. Grandjean, J. et al. Common functional networks in the mouse brain revealed by multi-centre resting-state fMRI analysis. NeuroImage **205**, 116278 (2020).
155. Lake, E. M. R. et al. Simultaneous cortex-wide fluorescence Ca2+ imaging and whole-brain fMRI. Nat Methods **17**, 1262–1271 (2020).
156. Bakker, R., Tiesinga, P. & Kötter, R. The Scalable Brain Atlas: Instant Web-Based Access to Public Brain Atlases and Related Content. Neuroinform **13**, 353–366 (2015).

157. Fulcher, B. D., Murray, J. D., Zerbi, V. & Wang, X.-J. Multimodal gradients across mouse cortex. Proceedings of the National Academy of Sciences **116**, 4689–4695 (2019).
158. Wang, Q. et al. The Allen Mouse Brain Common Coordinate Framework: A 3D Reference Atlas. Cell **181**, 936-953.e20 (2020).
159. Lein, E. S. et al. Genome-wide atlas of gene expression in the adult mouse brain. Nature **445**, 168–176 (2007).
160. Markello, R. D. & Misic, B. Comparing spatial null models for brain maps. NeuroImage **236**, 118052 (2021).
161. Váša, F. et al. Adolescent tuning of association cortex in human structural brain networks. Cerebral Cortex **28**, 281–294 (2018).
162. Pang, J. C. et al. Reply to: Commentary on Pang et al. (2023) Nature. 2023.10.06.560797 Preprint at https://doi.org/10.1101/2023.10.06.560797 (2023).
163. Bazinet, V., Liu, Z.-Q. & Misic, B. The effect of spherical projection on spin tests for brain maps. 2024.12.15.628553 Preprint at https://doi.org/10.1101/2024.12.15.628553 (2024).
164. Kondo, S. & Miura, T. Reaction-Diffusion Model as a Framework for Understanding Biological Pattern Formation. Science **329**, 1616–1620 (2010).
165. Krause, A. L., Gaffney, E. A., Maini, P. K. & Klika, V. Introduction to 'Recent progress and open frontiers in Turing's theory of morphogenesis'. Philosophical Transactions of the Royal Society A: Mathematical, Physical and Engineering Sciences **379**, 20200280 (2021).
166. Gierer, A. & Meinhardt, H. A theory of biological pattern formation. Kybernetik **12**, 30–39 (1972).
167. Green, J. B. A. & Sharpe, J. Positional information and reaction-diffusion: two big ideas in developmental biology combine. Development **142**, 1203–1211 (2015).
168. Fenlon, L. R. Timing as a Mechanism of Development and Evolution in the Cerebral Cortex. Brain Behav Evol **97**, 8–32 (2022).